Well-controlled 3D flower-like CoP$_3$/CeO$_2$/C heterostructures as bifunctional oxygen electrocatalysts for rechargeable Zn-air batteries

Jinmei Li [a], Yumao Kang [b], Ziqiang Lei [b], Peng Liu [a,*]

[a] State Key Laboratory of Applied Organic Chemistry and Key Laboratory of Nonferrous Metal Chemistry and Resources Utilization of Gansu Province, College of Chemistry and Chemical Engineering, Lanzhou University, Lanzhou 730000, China
[b] Key Laboratory of Eco-functional Polymer Materials of the Ministry of Education, Key Laboratory of Eco-environmental Polymer Materials of Gansu Province, College of Chemistry and Chemical Engineering, Northwest Normal University, Lanzhou 730070, China

A B S T R A C T

Recently, transition metal phosphides (TMPs) have emerged as robust electrocatalysts for rechargeable Zn-air batteries, but their electrocatalytic performance needs further improvements. Herein, well-controlled 3D flower-like CoP$_3$/CeO$_2$/C heterostructures are developed via a pyrolysis-phosphorization strategy, with 3D CeO$_2$ nanoflowers as promoters. The resultant CoP$_3$/CeO$_2$/C heterostructures exhibit high electrocatalytic activity in both oxygen evolution reaction (OER) and oxygen reduction reaction (ORR). Owing to the large specific surface area and enhanced electrical conductivity, the CoP$_3$/CeO$_2$/C-2 catalyst delivers a small overpotential (339.2 mV at 10 mA cm^{-2}) for the OER and a high half-wave potential for the ORR, which are superior to its counterparts. More importantly, it also demonstrates robust stability in OER and ORR. The CoP$_3$/CeO$_2$/C-2-based rechargeable Zn-air battery yields large power density (150.0 mW cm^{-2}), high energy density (871.3 Wh kg$_{Zn}^{-1}$), and excellent cycling stability.

1. Introduction

The aggravated energy consumption and environmental deterioration have greatly stimulated the pursuit of sustainable energy conversion and storage devices, for instance, water-splitting, fuel cells, and rechargeable metal-air batteries [1–4]. As one of the promising candidates, Zn-air batteries have attracted tremendous interest due to their merits of low cost, high theoretical energy density (1086 Wh kg^{-1}), and environmental benignity [5,6]. However, their widespread applications are heavily hampered by sluggish electrocatalytic reactions, including oxygen evolution reaction (OER) and oxygen reduction reaction (ORR) [7]. Although noble metal-based materials (e.g., Ru-/Ir-based composites and Pt-based compounds) are considered to be the benchmark catalysts for Zn-air batteries, the high cost, earth-limited availability, and limited stability severely hinder their potential deployment at any appreciable scale [8,9]. In this regard, it is crucial to design and develop cost-effective and durable bifunctional oxygen electrocatalysts for Zn-air batteries.

Nowadays, noble metal oxides-based catalysts with low noble metal loading [10,11] and transition metal-based catalysts (e.g., metal-organic framework (MOF)-derived single-atom catalysts [12,13],

Fe-Ni-Mn-based compounds [14], metal-nitrogen-carbon (M-N-C) catalysts [15,16], and transition metal compounds [17]) show great potential in OER and ORR attributed to their relatively low cost and high electrocatalytic activity. In particular, transition metal phosphides (TMPs) have achieved great progress in electrocatalysts [18–20]. Tremendous research efforts have demonstrated that the incorporation of negatively charged P with transition metals can limit the electron delocalization of metals, leading to the co-existence of covalent and ionic characteristics in the M-P bond. The strong M-P bond may endow TMPs with enhanced thermal and chemical stabilities [21,22]. Meanwhile, P can also reduce the energy gap of molecular orbitals, which plays a significant role in electrocatalysis [23]. Among the various TMPs, cobalt phosphides (including Co$_2$P [24], CoP [25,26], CoP$_2$ [27], and CoP$_3$ [28]) represent a class of robust candidates with earth abundance, tunable electronic structure, and high catalytic activity in the energy field [18,29,30]. Especially, CoP$_3$ with high phosphorous content can offer more active sites for electrocatalytic reactions [31]. For example, Zhang et al. reported a self-supporting bifunctional catalyst composed of amorphous and porous CoP$_3$ nanoneedle, which showed excellent catalytic performance for hydrogen evolution reaction (HER) and OER [32]. Lin et al. synthesized Fe-doped skutterudite-type CoP$_3$

nanoneedles with satisfactory HER and OER performance [33]. Despite these efforts, the catalytic performance of most cobalt phosphides for OER and ORR still lags far behind noble metal-based catalysts [34,35].

It has been recognized as an effective strategy to improve the electrocatalytic activity and long-term stability of CoP_3 by introducing oxygen vacancy to modulate the electronic structure of CoP_3. As demonstrated by Li and co-workers [36], the electrocatalytic activity of Fe-Ni_5P_4/NiFeOH nanosheets could be significantly improved by the abundant oxygen vacancies in NiFeOH. Currently, CeO_2 has been proposed as a promising promoter of electrocatalysts due to its rich oxygen vacancies and unique chemical properties [29]. The transformation between Ce^{3+} and Ce^{4+} can provide reversible oxygen ion exchange and act as an efficient buffer for oxygen storage and release [37,38]. Besides, CeO_2 can also optimize the surface-active sites and enrich the defect structures of catalysts [39]. Meanwhile, CeO_2 holds good stability in alkaline electrolytes, which is also conducive to the electrocatalytic process [40]. Therefore, it is expected to adjust the electronic structure of CoP_3 and generate additional active sites to boost OER/ORR electrocatalytic performance by cooperating CoP_3 with CeO_2.

Besides, it is also an important aspect to maximize the catalytic activity of CoP_3, by tailoring the particle size and morphology of the CoP_3. Recent investigations demonstrate that the electrocatalytic activity of catalysts can be improved by reducing the particle size of active metal [41]. The smaller nanoparticles in catalysts deliver a larger surface-to-volume ratio and contact area of the electrolyte/catalyst, thereby providing more active sites and improving the utilization efficiency of active metal atoms during electrocatalytic reactions [42,43]. Given the above considerations, it is highly attractive but still challenging to rational design CoP_3/CeO_2 hybrids with optimized electronic structure and well-controlled morphology.

Herein, 3D flower-like CoP_3/CeO_2/C heterostructures are fabricated via a pyrolysis-phosphorization process (Scheme 1), with MOF-derived 3D CeO_2 nanoflowers as promoters to adjust the electronic structure and nanostructure of CoP_3, to improve its electrocatalytic performance. Interestingly, the morphology, surface area, and metal content of the CoP_3/CeO_2/C heterostructures can be effectively tuned by altering the molar ratio of Co and Ce (Co^{2+}/Ce^{3+}). By optimizing the electronic structure of CoP_3/CeO_2/C heterostructures, the OER and ORR activities

of CoP_3/CeO_2/C-2 are significantly enhanced in comparison with individual CoP_3/C and CeO_2/C. As expected, the as-prepared CoP_3/CeO_2/C-2 demonstrates promising bifunctional electrocatalytic activities, with a small overpotential of 339.2 mV at 10 mA cm^{-2} for the OER and a high half-wave potential for ORR, outperforming the counterparts of CoP_3/C and CeO_2/C. Additionally, the long-term stability of the CoP_3/CeO_2/C-2 is greatly improved for both OER and ORR. More importantly, CoP_3/CeO_2/C-2-based aqueous rechargeable Zn-air battery delivers high power density of 150.0 mW cm^{-2} and energy density of 871.3 Wh kg_{Zn}^{-1}, robust cycling stability, and improved energy efficiency. And the assembled flexible Zn-air batteries exhibit promising applications for wearable devices.

2. Experimental section

2.1. Synthesis of Ce-MOF and Co-MOF

The 3D flower-like Ce-MOF was synthesized by a hydrothermal method according to a previous procedure with some modifications [44]. Typically, 1.5 mmol Ce(NO_3)$_3$·$6H_2O$ was dissolved in 30 mL N, N-dimethylformamide (DMF) to form a clear solution (A). Then 1.5 mmol 1,2,4,5-benzenetetracarboxylic acid (H_4BTC) was dissolved in 15 mL DMF to form a uniform solution (B). Afterward, solution B was added dropwise to solution A with vigorous stirring. Subsequently, the mixed solution was heated at 160 ℃ for 24 h in a Teflon-lined autoclave. After the reaction, the Ce-MOF was gained as a white powder, by rinsing with DMF and methanol and drying at 60 ℃ overnight.

The Co-MOF was prepared using the same procedure with Co (NO_3)$_2$·$6H_2O$ instead of Ce(NO_3)$_3$·$6H_2O$. The Co^{2+} precursors could coordinate with H_4BTC to form an oval-shaped Co-MOF.

2.2. Synthesis of CoCe-MOFs

The CoCe-MOFs were prepared with a similar procedure as the Ce-MOF. Typically, 1.5 mmol mixture of Co(NO_3)$_2$·$6H_2O$ and Ce (NO_3)$_3$·$6H_2O$ with different molar ratios of Co^{2+}/Ce^{3+} was dissolved in 30 mL DMF. Next, 15 mL DMF solution containing 1.5 mmol H_4BTC was added dropwise with vigorous stirring. Then the mixed solution was
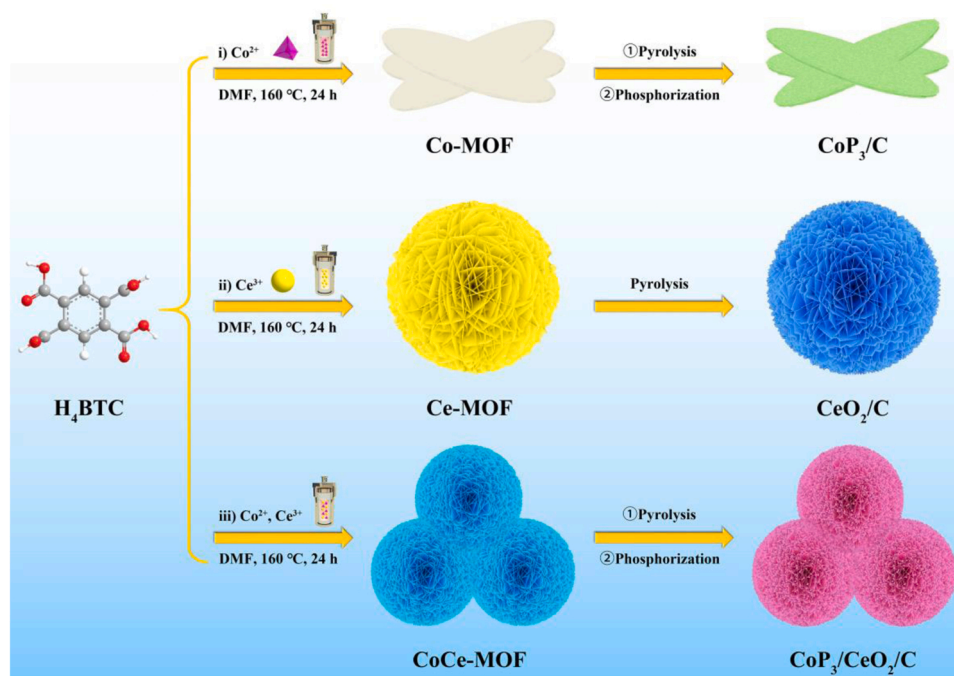
Scheme 1. Schematic illustration of the synthesis of CoP_3/C, CeO_2/C, and CoP_3/CeO_2/C.

sealed in a Teflon-lined autoclave for hydrothermal treatment at 160 ℃ for 24 h. The precipitates were collected by centrifugation, washed several times with DMF and methanol, and dried at 60 ℃ overnight. According to the Co^{2+}/Ce^{3+} molar ratio of 5:1, 3:1, 1:1, 1:3, and 1:5, the products were named as CoCe-MOF-1, CoCe-MOF-2, CoCe-MOF-3, CoCe-MOF-4, and CoCe-MOF-5, respectively.

2.3. Preparation of $CoP_3/CeO_2/C$ heterostructures, CoP_3/C, and CeO_2/C

The $CoP_3/CeO_2/C$ heterostructures were fabricated via the sequential strategy of high-temperature pyrolysis and low-temperature phosphorization. Specifically, the as-prepared CoCe-MOF-1, CoCe-MOF-2, CoCe-MOF-3, CoCe-MOF-4, and CoCe-MOF-5 were heated at 700 ℃ for 2 h (5 ℃ min^{-1}) in a tube furnace under the N_2 atmosphere. After cooling down, 0.05 g above samples and 0.5 g NaH_2PO_2 were separately loaded in two porcelain boats and put in a tube furnace at a distance of 10 cm. Then, the samples were treated at 300 ℃ (1 ℃ min^{-1}) under the N_2 atmosphere for 2 h. The resulting products were named as $CoP_3/CeO_2/C$-1, $CoP_3/CeO_2/C$-2, $CoP_3/CeO_2/C$-3, $CoP_3/CeO_2/C$-4, and $CoP_3/CeO_2/C$-5, respectively.

For comparison, the CoP_3/C was prepared by pyrolysis of Co-MOF with the same procedure, while the CeO_2/C was prepared by pyrolysis of Ce-MOF at 700 ℃ for 2 h (5 ℃ min^{-1}) under the N_2 atmosphere.

3. Results and discussion

3.1. Characterization of catalysts

The morphology and structure of the CoP_3/C, CeO_2/C, and $CoP_3/CeO_2/C$ heterostructures were characterized with scanning electron microscopy (SEM) technique. As shown in Fig. 1a, the CoP_3/C with oval-shaped structure was composed of many irregular nanoparticles (NPs). In comparison with the CoP_3/C, the CeO_2/C presented 3D flower-like structure with a smooth surface (Fig. 1b). The interlaced sheet structure of CeO_2/C offered a large specific surface area and an extensive interface between CeO_2/C catalyst and electrolyte, thus ensuring fast charge/mass transfer during electrocatalysis. Interestingly, it was found that the morphology of the $CoP_3/CeO_2/C$ heterostructures was closely related to the content of Ce. As displayed in Fig. 1c and d, the $CoP_3/CeO_2/C$-1 and $CoP_3/CeO_2/C$-2 showed a smaller size of nanosheets and flower-like morphology, which was conducive to the formation of small and uniform NPs. When the Co^{2+}/Ce^{3+} molar ratio was 1:1, the pores formed on the $CoP_3/CeO_2/C$-3 surface became more compact, and the size of flower-like morphology began to increase significantly (Fig. 1e). With the further increase of Ce concentration, the $CoP_3/CeO_2/C$-4 and $CoP_3/CeO_2/C$-5 exhibited a similar flower-like morphology as CeO_2/C (Fig. 1f and g). These results indicated that the coordination competition between Co^{2+} and Ce^{3+} gave rise to the synthesis of CoCe-MOFs with tunable morphology, composition, and crystal structure, as evidenced by the SEM images (Fig. S1), energy-dispersive spectroscopy (EDS) results (Fig. S2), and powder X-ray diffraction (XRD) patterns (Fig. S3), respectively. CoP_3/C, CeO_2/C, and $CoP_3/CeO_2/C$ heterostructures perfectly inherited the morphology of MOF precursors after the pyrolysis-phosphorization process. Therefore, the CoCe-MOFs could be used as ideal precursors to fabricate $CoP_3/CeO_2/C$ heterostructures. Furthermore, the elemental mapping images of the $CoP_3/CeO_2/C$-2 revealed that C, O, P, Co, and Ce elements were uniformly distributed over the entire architecture (Fig. 1h).

The microstructural features of as-prepared catalysts were analyzed using transmission electron microscopy (TEM) technique to investigate the structural changes at different precursor ratios. As shown in Fig. S4, the flower-like morphology of CeO_2/C and $CoP_3/CeO_2/C$ heterostructures could be observed, which was consistent with the characterization results of SEM. Meanwhile, some broken nanosheets were present around CeO_2/C and $CoP_3/CeO_2/C$ heterostructures. In addition, the TEM images indicated that CeO_2/C and $CoP_3/CeO_2/C$
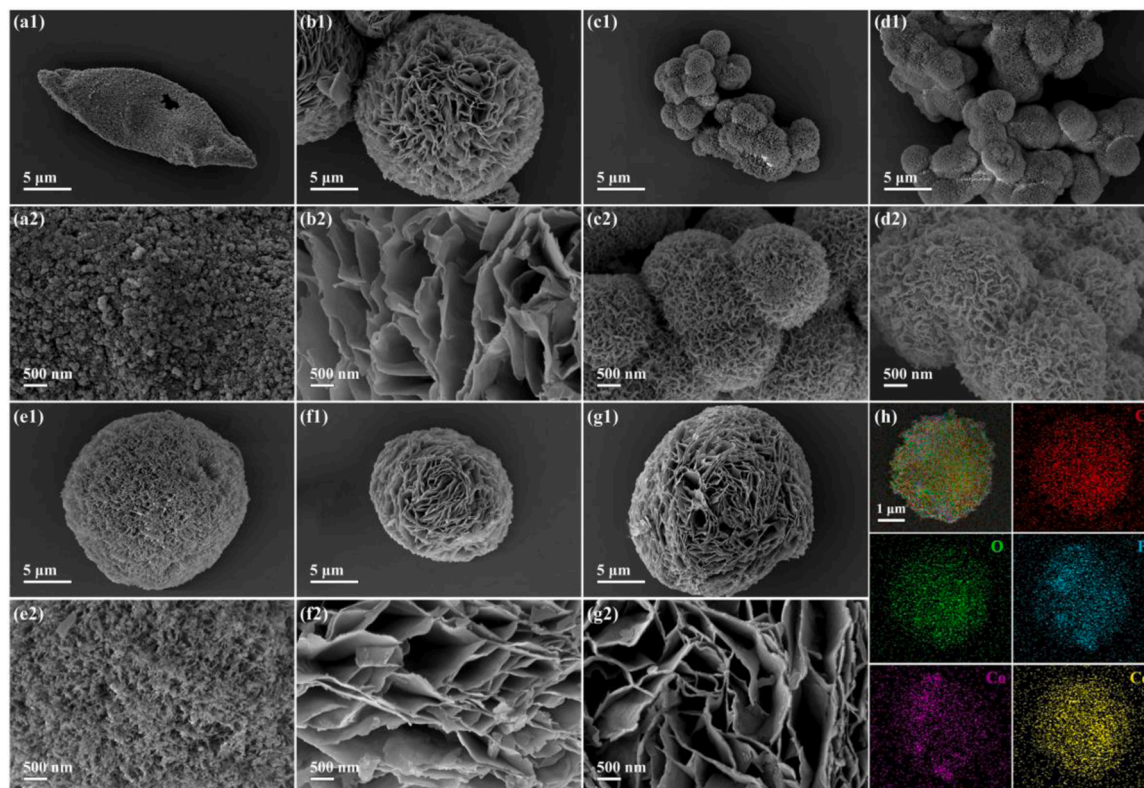
Fig. 1. Typical SEM images of (a) CoP_3/C, (b) CeO_2/C, (c) $CoP_3/CeO_2/C$-1, (d) $CoP_3/CeO_2/C$-2, (e) $CoP_3/CeO_2/C$-3, (f) $CoP_3/CeO_2/C$-4, and (g) $CoP_3/CeO_2/C$-5. (h) Elemental mapping distributions for C, O, P, Co, and Ce of the $CoP_3/CeO_2/C$-2.

heterostructures were not hollow structures. As shown in Fig. 2a and Fig. S5a, the CoP$_3$ NPs with inhomogeneous size and serious agglomeration were observed on the CoP$_3$/C, which was consistent with the SEM result (Fig. 1a). TEM image (Fig. 2b) illustrated that the CeO$_2$/C was composed of many irregular ultrathin nanosheets, and abundant small CeO$_2$ NPs were evenly distributed and anchored on its surface (Fig. S5b). Comparatively, aggregation of CoP$_3$/CeO$_2$/C-1 NPs occurred due to the introduction of CeO$_2$, accompanied by smaller nanosheets (Fig. 2c). Increasing the content of Ce, the CoP$_3$/CeO$_2$/C-2 (Fig. 2d) and CoP$_3$/CeO$_2$/C-3 (Fig. 2e) exhibited both rod-like and sheet-like structures without obvious agglomeration of NPs on the surface. Meanwhile, it could be seen that the high Ce content could significantly increase CeO$_2$ nanosheets in the CoP$_3$/CeO$_2$/C-4 (Fig. 2f). Further increasing the content of Ce, the CoP$_3$/CeO$_2$/C-5 (Fig. 2g) displayed a similar microstructure as CeO$_2$/C, indicating that the structure of CoP$_3$/CeO$_2$/C-5 was mainly determined by the Ce concentration. In addition, TEM results demonstrated that the introduction of CeO$_2$ could remarkably reduce the particle size of CoP$_3$/CeO$_2$/C heterostructures. The high-resolution TEM (HRTEM) image of the CoP$_3$/CeO$_2$/C-2 (Fig. 2h) showed the connected crystal lattices of CeO$_2$ (*200*) and CoP$_3$ (*310*) planes, which could be confirmed by the fast Fourier transform (FFT) patterns (the cyan rectangle from the region (I) and yellow rectangle from the region (II) in Fig. 2h), suggesting the formation of heterointerface. The corresponding inverse FFT (IFFT) patterns and the line profiles (Fig. 2i and j) revealed 0.266 and 0.251 nm spacings, which were associated with the (*200*) crystal plane of CeO$_2$ and (*310*) crystal plane of CoP$_3$, respectively.

The wettability of the CoP$_3$/C, CeO$_2$/C, and CoP$_3$/CeO$_2$/C heterostructures was assessed by static water contact angle (CA) measurements (Fig. S6). Compared with the CoP$_3$/C with a CA of 33.8°, the CeO$_2$/C exhibited superhydrophilic properties with a CA of 0°. Notably, it was found that the CA value of the CoP$_3$/CeO$_2$/C heterostructures gradually decreased with increasing content of Ce, indicating the presence of CeO$_2$ could greatly improve surface hydrophilicity. Such a hydrophilic surface of the CoP$_3$/CeO$_2$/C heterostructures helped to enhance the contact between electrolyte and electrocatalyst, thus facilitating the transport of electrolyte [45]. Therefore, by optimizing the Co^{2+}/Ce^{3+} molar ratios, the CoP$_3$/CeO$_2$/C-2 heterostructure with uniform particle size and favorable hydrophilicity could be obtained, leading to enhanced electrocatalytic OER performance.

The phase structure of precursors and as-prepared catalysts was investigated by XRD. As displayed in Fig. 3a, the diffraction peaks of the CoP$_3$/C located at 28.1°, 32.6°, 40.3°, 43.8°, 47.2°, and 56.0° corresponded to the (*211*), (*220*), (*222*), (*321*), (*400*), and (*332*) planes of CoP$_3$ (JCPDS No. 27-1121), respectively, indicating the formation of CoP$_3$ phase in the CoP$_3$/C catalyst. Four weak diffraction peaks at about 27.7°, 30.5°, 68.4°, and 75.4° could be indexed to the (*104*), (*210*), (*416*), and (*336*) planes of carbon (JCPDS No. 22–1069), respectively. For the CeO$_2$/C, the diffraction peaks located at 28.5°, 33.0°, 47.3°, 56.0°, 59.0°, 69.2°, 76.8°, 78.8°, and 88.5° could be assigned to the (*111*), (*200*), (*220*), (*311*), (*222*), (*400*), (*331*), (*420*), and (*422*) planes of CeO$_2$ (JCPDS No. 81-0792), respectively. More interestingly, the representative diffraction peaks of both CoP$_3$ and CeO$_2$ were observed in the different CoP$_3$/CeO$_2$/C heterostructures, further confirming that the CoP$_3$/CeO$_2$/C heterostructures could be obtained from CoCe-MOFs via the proposed pyrolysis-phosphorization process.

In the Raman spectra (Fig. 3b), two prominent peaks of the D band (disordered carbon) and G band (graphitic carbon) could be observed at 1343 and 1581 cm^{-1}, respectively. The intensity ratios (I_D/I_G) were calculated using the integral areas of the D band and G band to evaluate the structural defects of catalysts [46,47]. Through Lorentzian curve-fitting (Fig. S7a-g), it was found that the CoP$_3$/C and CeO$_2$/C displayed the same I_D/I_G ratio of 2.16, indicating a similar defect level. Compared with the CoP$_3$/C and CeO$_2$/C, the decreased I_D/I_G ratios for CoP$_3$/CeO$_2$/C-1 (1.76), CoP$_3$/CeO$_2$/C-2 (1.72), and CoP$_3$/CeO$_2$/C-3
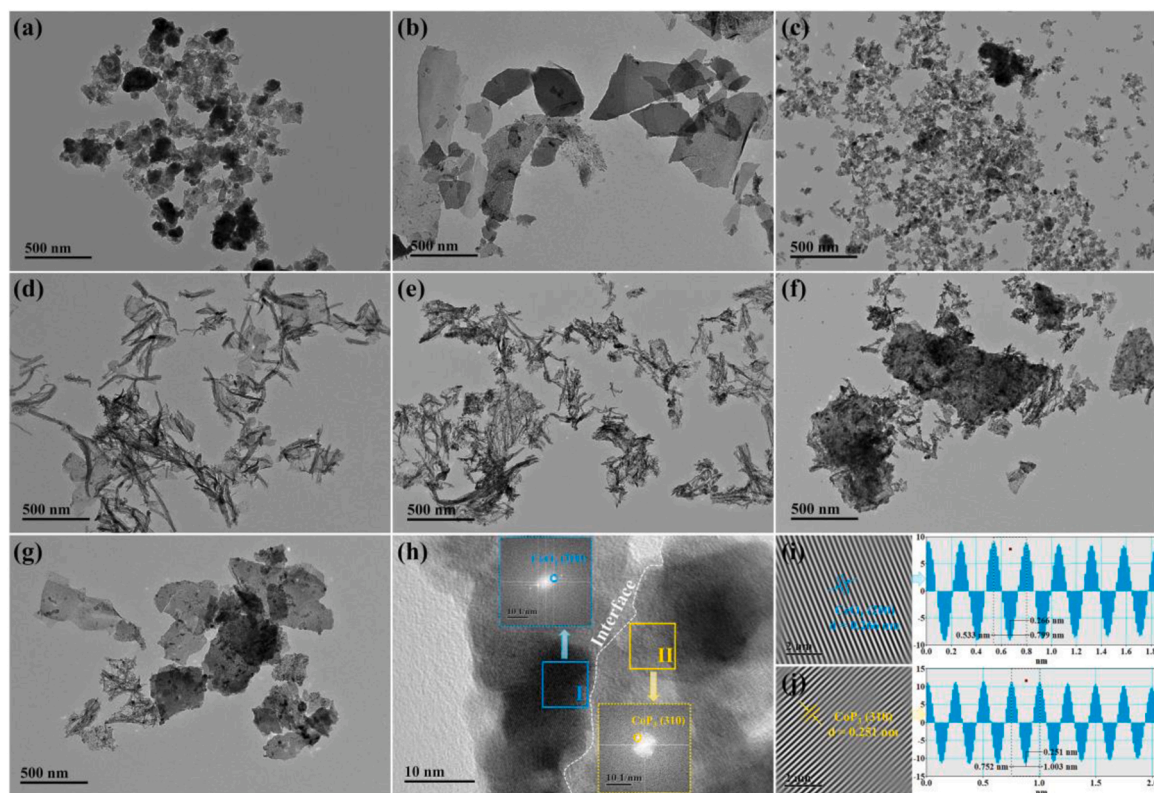
Fig. 2. Typical TEM images of (a) CoP$_3$/C, (b) CeO$_2$/C, (c) CoP$_3$/CeO$_2$/C-1, (d) CoP$_3$/CeO$_2$/C-2, (e) CoP$_3$/CeO$_2$/C-3, (f) CoP$_3$/CeO$_2$/C-4, and (g) CoP$_3$/CeO$_2$/C-5. (h) HRTEM image of CoP$_3$/CeO$_2$/C-2, inset: FFT patterns from the region boxed by (I) cyan rectangle and (II) yellow rectangle in (h). (i) Corresponding IFFT pattern and the line profile of the region (I). (j) Corresponding IFFT pattern and the line profile of the region (II).
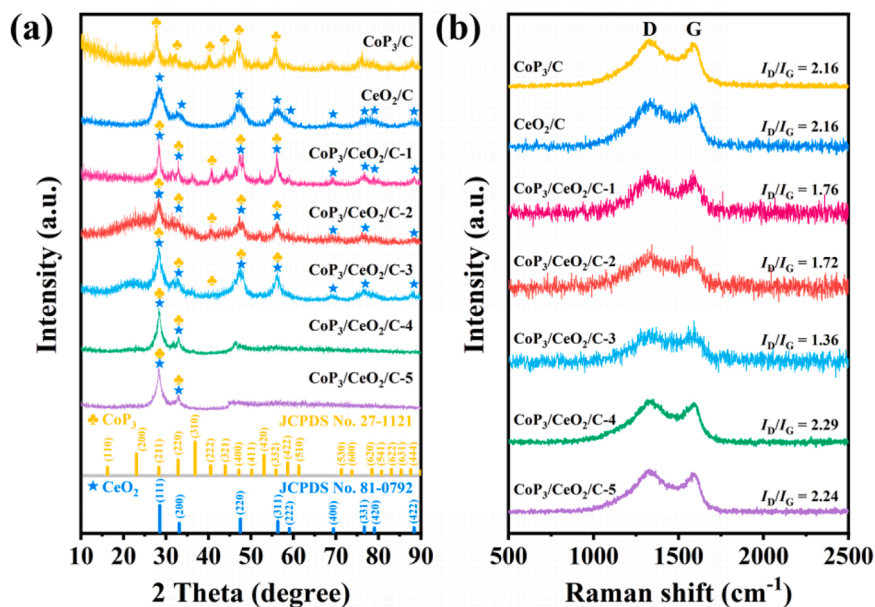
Fig. 3. (a) XRD patterns of CoP₃/C, CeO₂/C, and CoP₃/CeO₂/C heterostructures. (b) Raman spectra of CoP₃/C, CeO₂/C, and CoP₃/CeO₂/C heterostructures.

(1.36) were reasonably associated with their higher degree of graphitization, which could improve the electrical conductivity and corrosion resistance of carbon matrix, thereby boosting the electrocatalytic activity and stability of catalysts [48]. Yet, the CoP₃/CeO₂/C-4 (2.29) and CoP₃/CeO₂/C-5 (2.24) exhibited larger I_D/I_G ratios than the CeO₂/C, signifying the presence of more structural defects within the heterostructures. Generally, the structural defects could serve as efficient active sites to regulate the electronic structure of the metal and adjacent

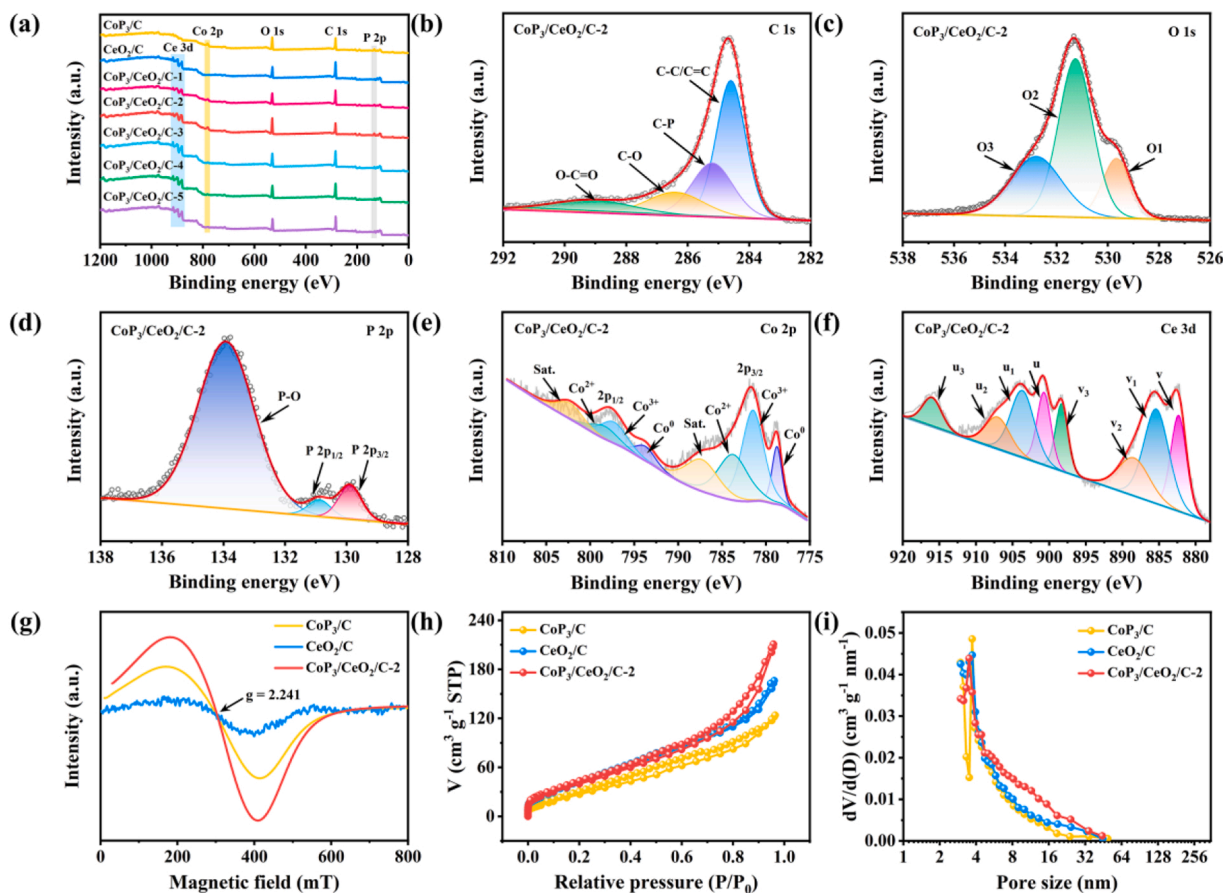**Fig. 4.** (a) XPS survey spectra of CoP₃/C, CeO₂/C, and CoP₃/CeO₂/C heterostructures. High-resolution (b) C 1 s, (c) O 1 s, (d) P 2p, (e) Co 2p, and (f) Ce 3d XPS spectra of CoP₃/CeO₂/C-2. (g) ESR spectra of CoP₃/C, CeO₂/C, and CoP₃/CeO₂/C-2. (h) N₂ adsorption-desorption isotherms of CoP₃/C, CeO₂/C, and CoP₃/CeO₂/C-2. (i) The corresponding BJH pore size distributions.

C atoms, which played a decisive role in promoting the electrocatalytic performance of catalysts [49,50]. Achieving a balance between desirable defects and the degree of graphitization might be more favorable for electrocatalysis [51].

X-ray photoelectron spectroscopy (XPS) was employed to analyze the surface electronic states of electrocatalysts. XPS survey spectra of the CoP_3/C, CeO_2/C, and CoP_3/CeO_2/C heterostructures confirmed the presence of P 2p, C 1 s, O 1 s, Co 2p, and Ce 3d signals (Fig. 4a). The corresponding surface atomic concentrations were listed in Table S1. In the high-resolution C 1 s XPS spectra (Fig. 4b and Fig. S8), the deconvoluted peaks at ~284.6, ~285.2, ~286.4, and ~289.0 eV were assigned to C−C/C═C, C−P, C−O, and O−C═O, respectively [52,53]. As presented in Table S2, the existence of C−P in CoP_3/C and CoP_3/CeO_2/C heterostructures indicated the successful P-doping. The high-resolution O 1 s XPS spectra (Fig. 4c and Fig. S9) could be deconvoluted into three peaks centered at ~529.6, ~531.2, and ~533.0 eV, corresponding to metal-oxygen (O1), oxygen vacancies (O2), and hydroxy or surface adsorbed oxygen (O3), respectively [37]. Notably, the percentage of O1 in a series of CoP_3/CeO_2/C heterostructures generally increased with a higher content of Ce. Meanwhile, the O1 peak of CoP_3/CeO_2/C heterostructures displayed a negative shift of ~0.1 eV compared with the CeO_2/C, which was ascribed to the strong electronic interaction between CoP_3 and CeO_2, indicating the formation of heterostructure [54]. Besides, in comparison with the CeO_2/C, the obtained O2 contents in the CoP_3/CeO_2/C heterostructures increased slightly, suggesting that the CoP_3/CeO_2/C heterostructures possessed more oxygen vacancies. As illustrated in Fig. 4d and Fig. S10, the high-resolution P 2p spectra showed three main peaks at ~129.8, ~130.7, and ~133.9 eV, which could be ascribed to the P $2p_{3/2}$, P $2p_{1/2}$, and oxidized P, respectively [29]. It was found that the P 2p peaks of CoP_3/CeO_2/C heterostructures were negatively shifted by ~0.2 eV relative to the CoP_3/C, revealing that a new equilibrium of the charge distribution was established between CoP_3 and CeO_2 with a heterostructure [55]. In the high-resolution XPS spectra of Co 2p (Fig. 4e, Fig. S11a and b), two pairs of doublet peaks located at 778–788 eV and 793–803 eV could be assigned to Co $2p_{3/2}$ and Co $2p_{1/2}$, respectively [56]. For the Co $2p_{3/2}$ spin-orbit, the Co^0, Co^{3+}, and Co^{2+} signal peaks were marked at ~778.8, ~781.5, and ~783.7 eV, respectively [5,57]. Two prominent shake-up satellites at ~787.5 and ~803.5 eV were also observed [58]. In addition, the Co 2p XPS spectra of the CoP_3/CeO_2/C-3, CoP_3/CeO_2/C-4, and CoP_3/CeO_2/C-5 showed a relatively weak intensity (Fig. S11c), due to the low content of Co species in heterostructures.

To gain more insight into the oxygen vacancies of the CoP_3/CeO_2/C heterostructures, the high-resolution Ce 3d XPS spectra were investigated, as shown in Fig. 4f and Fig. S12. More specifically, the peaks denoted as v_1 (~884.4 eV) and u_1 (~903.6 eV) were attributed to the Ce $3d_{5/2}$ and Ce $3d_{3/2}$ of Ce^{3+}, respectively, while the peaks denoted as v (~882.5 eV), v_2 (~888.9 eV), v_3 (~898.5 eV), u (~901.1 eV), u_2 (~908.1 eV), and u_3 (~916.6 eV) corresponded to the Ce^{4+} species in CeO_2 nanoflowers [59,60]. The Ce^{3+} species could offer charge compensation and generate rich oxygen vacancies [61,62], which were beneficial for providing more accessible active sites and modifying the electronic structure of CoP_3/CeO_2/C heterostructures, thus improving their electrocatalytic activities. [63]. To further reveal oxygen vacancies, electron spin resonance (ESR) measurements of the CoP_3/C, CeO_2/C, and CoP_3/CeO_2/C-2 were carried out. As shown in Fig. 4g, the nearly symmetric ESR signals around g = 2.241 were caught in CoP_3/C and CeO_2/C catalysts, indicating the existence of oxygen vacancies [29]. The intensity of the ESR peak of CoP_3/CeO_2/C-2 was significantly enhanced after the introduction of 3D CeO_2 nanoflowers, demonstrating that the heterostructure formed between CoP_3 and CeO_2 could introduce more oxygen vacancies in CoP_3/CeO_2/C-2.

The pore structures and specific surface area of as-prepared CoP_3/C, CeO_2/C, and CoP_3/CeO_2/C heterostructures were evaluated by N_2 adsorption-desorption analysis. As shown in Fig. 4h and Fig. S13, the isotherms for all the samples could be categorized as typical type IV

curves with H3 hysteresis loops, revealing the existence of mesoporous [64]. This result was well matched with the Barrett-Joyner-Halenda (BJH) pore size distribution curves (Fig. 4i and the insets in Fig. S13). As listed in Table S3, the pore sizes of the catalysts were mainly concentrated in the range of 3–4 nm. Based on Brunauer-Emmett-Teller (BET) method, the specific surface area was calculated as 107.72, 152.32, 87.21, 161.06, 66.84, 56.17, and 87.37 m^2 g^{-1} for CoP_3/C, CeO_2/C, CoP_3/CeO_2/C-1, CoP_3/CeO_2/C-2, CoP_3/CeO_2/C-3, CoP_3/CeO_2/C-4, and CoP_3/CeO_2/C-5, respectively. The CoP_3/CeO_2/C-2 exhibited a larger specific surface area than its counterparts, owing to its optimized morphology and microstructure. Such porous structures would be expected to provide more exposed active sites and abundant open channels for mass transfer [65,66]. Additionally, the difference in pore structures could be further perceived from the pore volume of CoP_3/CeO_2/C heterostructures. The CoP_3/CeO_2/C-1 (0.42 cm^3 g^{-1}), CoP_3/CeO_2/C-2 (0.33 cm^3 g^{-1}), and CoP_3/CeO_2/C-4 (0.38 cm^3 g^{-1}) showed bigger total pore volumes than CeO_2/C (0.26 cm^3 g^{-1}), CoP_3/C (0.19 cm^3 g^{-1}), CoP_3/CeO_2/C-3 (0.12 cm^3 g^{-1}), and CoP_3/CeO_2/C-5 (0.15 cm^3 g^{-1}), implying that the unique porous features of CoP_3/CeO_2/C heterostructures were related to their morphological evolution.

3.2. Electrocatalytic properties toward OER and ORR

To reveal the advantage of CoP_3/CeO_2/C heterostructures, the electrocatalytic performance of catalysts for the OER was evaluated using a three-electrode system. Fig. 5a presented the linear sweep voltammetry (LSV) curves of RuO_2, nickel foam (NF) substrate, CoP_3/C, CeO_2/C, and CoP_3/CeO_2/C heterostructures. Significantly, the CoP_3/CeO_2/C-2 exhibited high OER activity with a large current density of oxygen evolution and a low overpotential of 339.2 mV at 10 mA cm^{-2}, which outperformed the CoP_3/C (361.7 mV), CeO_2/C (404.1 mV), CoP_3/CeO_2/C-1 (346.7 mV), CoP_3/CeO_2/C-3 (374.1 mV), CoP_3/CeO_2/C-4 (395.4 mV), CoP_3/CeO_2/C-5 (423.5 mV), and NF (461.3 mV). The OER activity of the CoP_3/CeO_2/C-2 was comparable to the state-of-the-art RuO_2 catalyst (337.2 mV overpotential at 10 mA cm^{-2}). The reaction kinetics was then inspected by Tafel slopes. As expected, the Tafel slope of the CoP_3/CeO_2/C-2 (80 mV dec^{-1}) depicted in Fig. 5b and c was smaller than CoP_3/C (82 mV dec^{-1}), CeO_2/C (214 mV dec^{-1}), CoP_3/CeO_2/C-1 (111 mV dec^{-1}), CoP_3/CeO_2/C-3 (115 mV dec^{-1}), CoP_3/CeO_2/C-4 (141 mV dec^{-1}), CoP_3/CeO_2/C-5 (126 mV dec^{-1}), RuO_2 (120 mV dec^{-1}), and NF (138 mV dec^{-1}), suggesting a favorable OER kinetics [67]. The CoP_3/CeO_2/C-2 possessed the smallest Tafel slope in the CoP_3/CeO_2/C heterostructures, which might be attributed to the following reasons: (i) The charge redistribution at the interface of CoP_3/CeO_2 could optimize the electronic structure of the CoP_3/CeO_2/C-2, thus generating a favorable electronic microenvironment for the OER and promoting OER kinetics. (ii) Among the CoP_3/CeO_2/C heterostructures, the CoP_3/CeO_2/C-2 exhibited the largest surface area, which provided more exposed active sites and abundant open channels for charge/mass transport during the OER processes, facilitating OER kinetics. It could be seen from the histogram in Fig. 5c that the CoP_3/CeO_2/C-2 also achieved the lowest overpotential of 494.7 mV at 200 mA cm^{-2} among them, manifesting the markedly enhanced OER activity by optimizing the morphology and electronic structure of CoP_3/CeO_2/C heterostructures. Moreover, the OER performance of the CoP_3/CeO_2/C-2 was comparable or even superior to some of the recently reported Co-based or Ce-based catalysts (Table S4).

The charge-transfer kinetics of samples was examined by electrochemical impedance spectroscopy (EIS) analysis (Fig. 5d). An equivalent circuit (inset of Fig. 5d) was used to analyze the experimental impedance data and the parameters were summarized in Table S5. Notably, based on the Nyquist plots, the fitting results revealed that the solution resistance (R_s) of all the catalysts was similar. In addition, the solid-electrolyte interface resistance (R_f) of different CoP_3/CeO_2/C heterostructures decreased in comparison with the CeO_2/C, due to the lower interface resistance of CoP_3. Interestingly, the CoP_3/CeO_2/C-2 exhibited
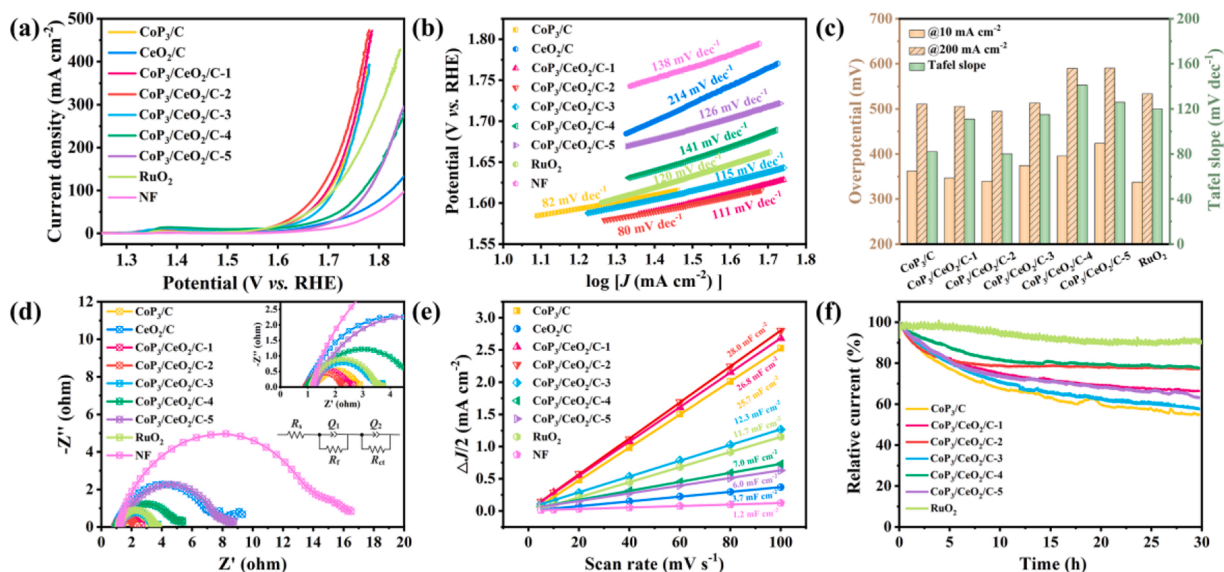
Fig. 5. Electrocatalytic performance of CoP_3/C, CeO_2/C, $CoP_3/CeO_2/C$ heterostructures, RuO_2, and NF for OER in O_2-saturated 1 M KOH solution. (a) LSV polarization curves. (b) The corresponding Tafel plots. (c) Performance statistics including overpotential at different current densities and Tafel plots. (d) The corresponding Nyquist plots. Inset: the enlarged profile of the Nyquist plots at high frequency and the equivalent circuit. (e) Capacitive current at 1.24 V (vs. RHE) against the scan rate. (f) Chronoamperometric response at a constant potential of 1.60 V (vs. RHE).

the smallest charge-transfer resistance (R_{ct}) of 1.57 Ω as compared to those of CoP_3/C (2.07 Ω), CeO_2/C (6.54 Ω), $CoP_3/CeO_2/C$-1 (1.76 Ω), $CoP_3/CeO_2/C$-3 (2.21 Ω), $CoP_3/CeO_2/C$-4 (3.85 Ω), $CoP_3/CeO_2/C$-5 (6.49 Ω), RuO_2 (2.94 Ω), and NF (13.63 Ω), demonstrating more efficient electron transfer between the $CoP_3/CeO_2/C$-2 and electrolyte during the OER process [68]. The above results verified that the introduction of 3D CeO_2 nanoflowers could significantly improve the electronic conductivity and charge transfer ability of $CoP_3/CeO_2/C$ heterostructures. Further, the double-layer capacitance (C_{dl}) of catalysts was obtained using cyclic voltammetry (CV) measurements with different scan rates (Fig. S14). As shown in Fig. 5e, the C_{dl} of the $CoP_3/CeO_2/C$-2 (28.0 mF cm^{-2}) was larger than those of CoP_3/C (25.7 mF cm^{-2}), CeO_2/C (3.7 mF cm^{-2}), $CoP_3/CeO_2/C$-1 (26.8 mF cm^{-2}), $CoP_3/CeO_2/C$-3 (12.3 mF cm^{-2}), $CoP_3/CeO_2/C$-4 (7.0 mF cm^{-2}), $CoP_3/CeO_2/C$-5 (6.0 mF cm^{-2}), RuO_2 (11.7 mF cm^{-2}), and NF (1.2 mF cm^{-2}). As depicted in Fig. S15a, the value of ECSA was calculated to be 21.4, 3.1, 22.3, 23.3, 10.3, 5.8, 5.0, and 9.8 cm^2 for CoP_3/C, CeO_2/C, $CoP_3/CeO_2/C$-1, $CoP_3/CeO_2/C$-2, $CoP_3/CeO_2/C$-3, $CoP_3/CeO_2/C$-4, $CoP_3/CeO_2/C$-5, and RuO_2, respectively. The ECSA of the $CoP_3/CeO_2/C$-2 was around 2.4 times higher than that of RuO_2, indicating more accessible active sites in the $CoP_3/CeO_2/C$-2 [69,70]. Fig. S15b showed that the mass activity of catalysts increased with increasing overpotential. The $CoP_3/CeO_2/C$-2 delivered a high mass activity reaching 787.9 mA mg^{-1} at an overpotential of 550 mV, which indicated the excellent OER performance of the $CoP_3/CeO_2/C$-2.

The long-term stabilities of as-prepared catalysts toward OER were investigated by chronoamperometric method at a constant potential of 1.60 V, as shown in Fig. 5f. After continuous testing for 30 h, the residual current percentages of CoP_3/C, $CoP_3/CeO_2/C$-1, $CoP_3/CeO_2/C$-2, $CoP_3/CeO_2/C$-3, $CoP_3/CeO_2/C$-4, $CoP_3/CeO_2/C$-5, and RuO_2 were 55.2 %, 66.4%, 77.7 %, 57.6 %, 77.1 %, 63.3 %, and 90.3 %, respectively. Moreover, the $CoP_3/CeO_2/C$-2 was able to maintain a high relative potential of 59.0 % even after 30 h of testing in 6 M KOH (Fig. S16), manifesting its good stability. Further, as shown in Fig. S17a and b, the LSV polarization curves of the $CoP_3/CeO_2/C$-2 and RuO_2 displayed a slight decay of the current density after 3000 CV cycles compared with the initial curves. This result indicated that the $CoP_3/CeO_2/C$-2 exhibited robust durability during the OER process [71], which was comparable to RuO_2. The structural stability of the $CoP_3/CeO_2/C$-2 could be

confirmed by SEM, TEM, XRD, Raman, and XPS tests after 30 h of stability testing. As depicted in Fig. S18, only slight agglomeration was observed in the morphology of $CoP_3/CeO_2/C$-2. TEM image showed that the $CoP_3/CeO_2/C$-2 still maintained both rod-like and sheet-like structures (Fig. S19a). Meanwhile, HRTEM image and IFFT patterns further confirmed the presence of CeO_2 (*200*) and CoP_3 (*310*) planes (Fig. S19b–d). In addition, the XRD patterns and Raman spectra of $CoP_3/CeO_2/C$-2 were almost unchanged (Fig. S20). The results of the high-resolution XPS spectra (Fig. S21) indicated that the content of oxygen vacancies in the $CoP_3/CeO_2/C$-2 was not significantly reduced after stability testing. The absence of P 2p$_{3/2}$, P 2p$_{1/2}$, and Co^0 signal peaks was observed, which could be attributed to the presence of a phase change of $CoP_x \to Co_3O_4 \to CoOOH$ during the OER process [72]. Notably, no significant changes in the Ce^{3+} and Ce^{4+} signal peaks were observed, further indicating the good stability of CeO_2. These results indicated that $CoP_3/CeO_2/C$-2 possessed good structural stability.

The ORR activity of the CoP_3/C, CeO_2/C, and $CoP_3/CeO_2/C$ heterostructures was further evaluated by rotating disk electrode (RDE) testing in O_2-saturated 0.1 M KOH solution. The onset potential (E_{onset}) of catalysts was obtained by a second-order discrete differentiation method (Fig. S22) [73]. As shown in Fig. 6a, LSV curves displayed that the CoP_3/C and CeO_2/C exhibited remarkably different ORR behavior. The CoP_3/C delivered a lower E_{onset} of 0.778 V and half-wave potential ($E_{1/2}$) of 0.658 V compared with the CeO_2/C (0.780 V and 0.684 V), suggesting an inferior ORR performance. Interestingly, the $CoP_3/CeO_2/C$-2 possessed higher E_{onset} of 0.802 V and $E_{1/2}$ of 0.752 V (Fig. 6b), which surpassed those of $CoP_3/CeO_2/C$-1 (0.789 V and 0.737 V), $CoP_3/CeO_2/C$-3 (0.793 V and 0.694 V), $CoP_3/CeO_2/C$-4 (0.797 V and 0.707 V), and $CoP_3/CeO_2/C$-5 (0.770 V and 0.696 V). Although $CoP_3/CeO_2/C$-2 exhibited lower ORR activity compared to commercial Pt/C (0.879 V for E_{onset} and 0.855 V for $E_{1/2}$), it showed significantly enhanced ORR activity compared to CoP_3/C and CeO_2/C alone. The superior ORR activity of the $CoP_3/CeO_2/C$-2 could be attributed to its rich oxygen vacancies, optimized electronic structure, and large specific surface area, which provided more efficient active sites for the ORR. As disclosed by the Tafel plots (Fig. 6c), the $CoP_3/CeO_2/C$-2 afforded a Tafel slope of 58.0 mV dec^{-1}, which was smaller than those of CoP_3/C (82.5 mV dec^{-1}), CeO_2/C (81.5 mV dec^{-1}), $CoP_3/CeO_2/C$-1 (60.7 mV dec^{-1}), $CoP_3/CeO_2/C$-3 (66.1 mV dec^{-1}),
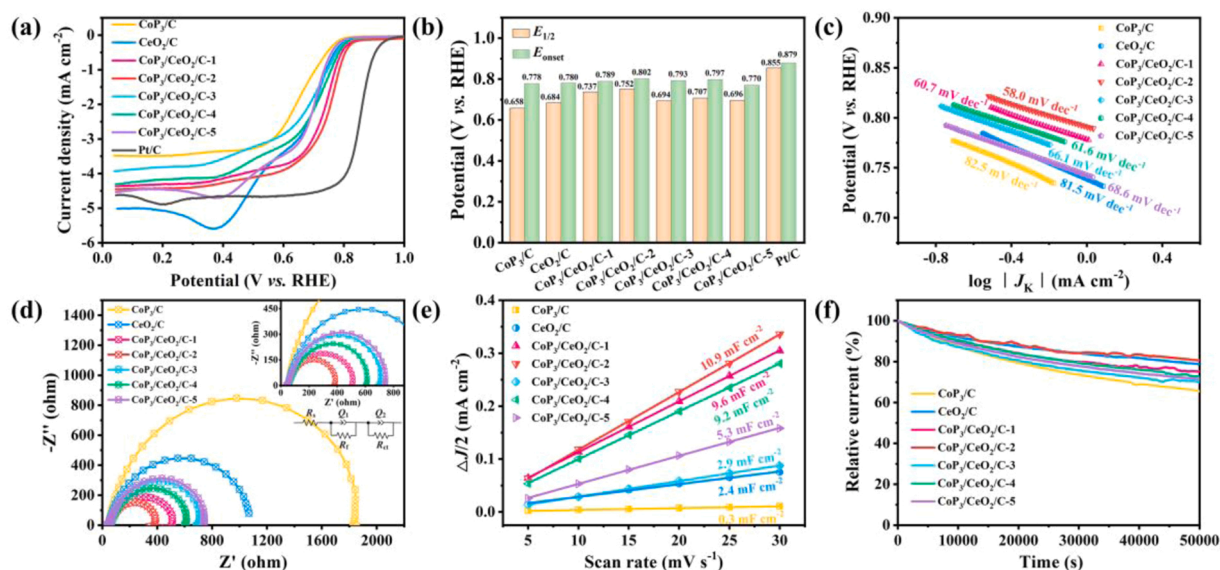
Fig. 6. The ORR performance of CoP_3/C, CeO_2/C, $CoP_3/CeO_2/C$ heterostructures, and Pt/C in O_2-saturated 0.1 M KOH solution. (a) LSV curves with the rotating speed of 1600 rpm at 10 mV s^{-1}. (b) The histogram of $E_{1/2}$ and E_{onset}. (c) The corresponding Tafel plots. (d) Nyquist plots in O_2-saturated 0.1 M KOH with the rotating speed of 1600 rpm at 0.80 V (vs. RHE). Inset: the enlarged profile of the Nyquist plots and the equivalent circuit. (e) Capacitive current at 0.55 V (vs. RHE) against the scan rate. (f) The i-t curves in 0.1 M KOH with a rotating speed of 1600 rpm at 0.65 V (vs. RHE).

$CoP_3/CeO_2/C$-4 (61.6 mV dec^{-1}), and $CoP_3/CeO_2/C$-5 (68.6 mV dec^{-1}), further confirming a faster ORR kinetics on the $CoP_3/CeO_2/C$-2 [74]. To explore the detailed reaction pathway for ORR, the LSV curves of samples at different rotating speeds were shown in Fig. S23. Obviously, the limiting current density in the LSV curves of as-prepared catalysts gradually increased upon increasing the rotating rate, implying that the ORR current was dependent on the O_2 diffusion [75]. In addition, the Koutecky-Levich (K-L) plots of all the catalysts illustrated good linearity from 0.3 to 0.5 V (inset of Fig. S23), demonstrating the first-order reaction kinetics for the ORR [76]. The average electron transfer number (n) was calculated to be ~3.13, ~3.50, ~3.73, ~3.88, ~3.56, ~3.64, and ~3.61 for CoP_3/C, CeO_2/C, $CoP_3/CeO_2/C$-1, $CoP_3/CeO_2/C$-2, $CoP_3/CeO_2/C$-3, $CoP_3/CeO_2/C$-4, and $CoP_3/CeO_2/C$-5, respectively. This revealed that the $CoP_3/CeO_2/C$-2 was closer to a four-electron pathway, whereas the other samples followed a similar ORR process combining two- and four-electron pathways. Likewise, the n values and the hydrogen peroxide (H_2O_2) yield were estimated via the rotating ring-disk electrode (RRDE) technique (Fig. S24a). As shown in Fig. S24b, the calculated n value of the $CoP_3/CeO_2/C$-2 was around 3.87, which was in good agreement with the RDE result. Furthermore, the H_2O_2 yield detected on $CoP_3/CeO_2/C$-2 was ~14.22 %, which was lower than CoP_3/C (~48.4 %) and CeO_2/C (~34.3 %), revealing the positive effect of $CoP_3/CeO_2/C$ heterostructure on ORR catalytic activity.

The EIS analysis was further carried out to confirm the significant role of $CoP_3/CeO_2/C$ heterostructure in the ORR. As indicated by the Nyquist plots (Fig. 6d), the $CoP_3/CeO_2/C$-2 exhibited better conductivity and faster kinetic performance with a low R_{ct} value of 312.8 Ω, which was smaller than those of CoP_3/C (1608.9 Ω), CeO_2/C (1057.3 Ω), $CoP_3/CeO_2/C$-1 (405.9 Ω), $CoP_3/CeO_2/C$-3 (637.6 Ω), $CoP_3/CeO_2/C$-4 (536.4 Ω), and $CoP_3/CeO_2/C$-5 (658.3 Ω). This result demonstrated that the electron transport ability of the CeO_2/C could be greatly improved by the integration with CoP_3. Compared with individual CeO_2/C and CoP_3/C, the cooperation of 3D CeO_2 nanoflowers with CoP_3 not only adjusted the morphology of $CoP_3/CeO_2/C$ heterostructures, but also created more oxygen vacancies and highly active sites for the ORR. The ECSA of different catalysts was checked by the C_{dl} to evaluate their intrinsic activity. Based on the CV curves recorded at various scan rates from 5 to 30 mV s^{-1} (Fig. S25a–g), the C_{dl} values were calculated, as depicted in Fig. 6e. As expected, the $CoP_3/CeO_2/C$-2 delivered the highest C_{dl} of 10.9 mF cm^{-2} and ECSA of 35.7 cm^2 (Fig. S25h) among

the as-prepared catalysts, revealing the enriched active sites in the $CoP_3/CeO_2/C$-2, which was attributed to its abundant oxygen vacancies and porous structure [77,78]. In addition to its high electrocatalytic performance, the $CoP_3/CeO_2/C$-2 also demonstrated superior stability and durability. After chronoamperometric test (Fig. 6f), the $CoP_3/CeO_2/C$-2 exhibited prominent stability with 80.6 % retention of the initial current, while the CoP_3/C, CeO_2/C, $CoP_3/CeO_2/C$-1, $CoP_3/CeO_2/C$-3, $CoP_3/CeO_2/C$-4, and $CoP_3/CeO_2/C$-5 retained 65.5 %, 78.8 %, 75.2 %, 70.1 %, 72.7 %, and 71.4 % of the initial current, respectively. Furthermore, the $CoP_3/CeO_2/C$-2 only displayed a slight shifting of the $E_{1/2}$ after 5000 CV cycles (Fig. S26), suggesting its high durability.

Overall, the $CoP_3/CeO_2/C$-2 catalyst delivered superior electrocatalytic properties toward OER and ORR. The bifunctional performance could be attributed to the following four aspects: 1) CoP_3 possessed high catalytic activity especially for the OER and CeO_2 showed good stability in alkaline environment, thereby endowing the $CoP_3/CeO_2/C$-2 with high OER performance. 2) Both CoP_3 and CeO_2 had rich oxygen vacancies, which could provide more accessible active sites and modify the electronic structure of $CoP_3/CeO_2/C$-2, leading to enhanced electronic conductivity and charge transfer kinetics. 3) The well-designed $CoP_3/CeO_2/C$-2 offered a large surface area and favorable hydrophilicity, thus providing more exposed active sites and efficient charge/mass transport channels during the OER processes. 4) The $CoP_3/CeO_2/C$-2 heterostructure might generate a synergistic effect between CoP_3 and CeO_2, which significantly improved the OER and ORR performance.

3.3. Rechargeable Zn-air battery performance

Inspired by the superior bifunctional performance of the $CoP_3/CeO_2/C$-2, an aqueous Zn-air battery was assembled, as schematically illustrated in Fig. 7a. A single $CoP_3/CeO_2/C$-2-based Zn-air battery displayed an open-circuit voltage (OCV) of 1.343 V (Fig. 7b). The red light-emitting-diode (LED) screen could be powered using three $CoP_3/CeO_2/C$-2-based Zn-air batteries connected in series (inset of Fig. 7b). As observed in Fig. 7c, the $CoP_3/CeO_2/C$-2-based Zn-air battery exhibited a better discharge performance than that of Pt/C-based Zn-air battery. Based on the discharge polarization curves (Fig. 7d), the $CoP_3/CeO_2/C$-2-based Zn-air battery presented a maximum power density of 150.0 mW cm^{-2}, which was higher than that Zn-air battery with Pt/C as the air cathode (117.9 mW cm^{-2}), suggesting the excellent dynamic
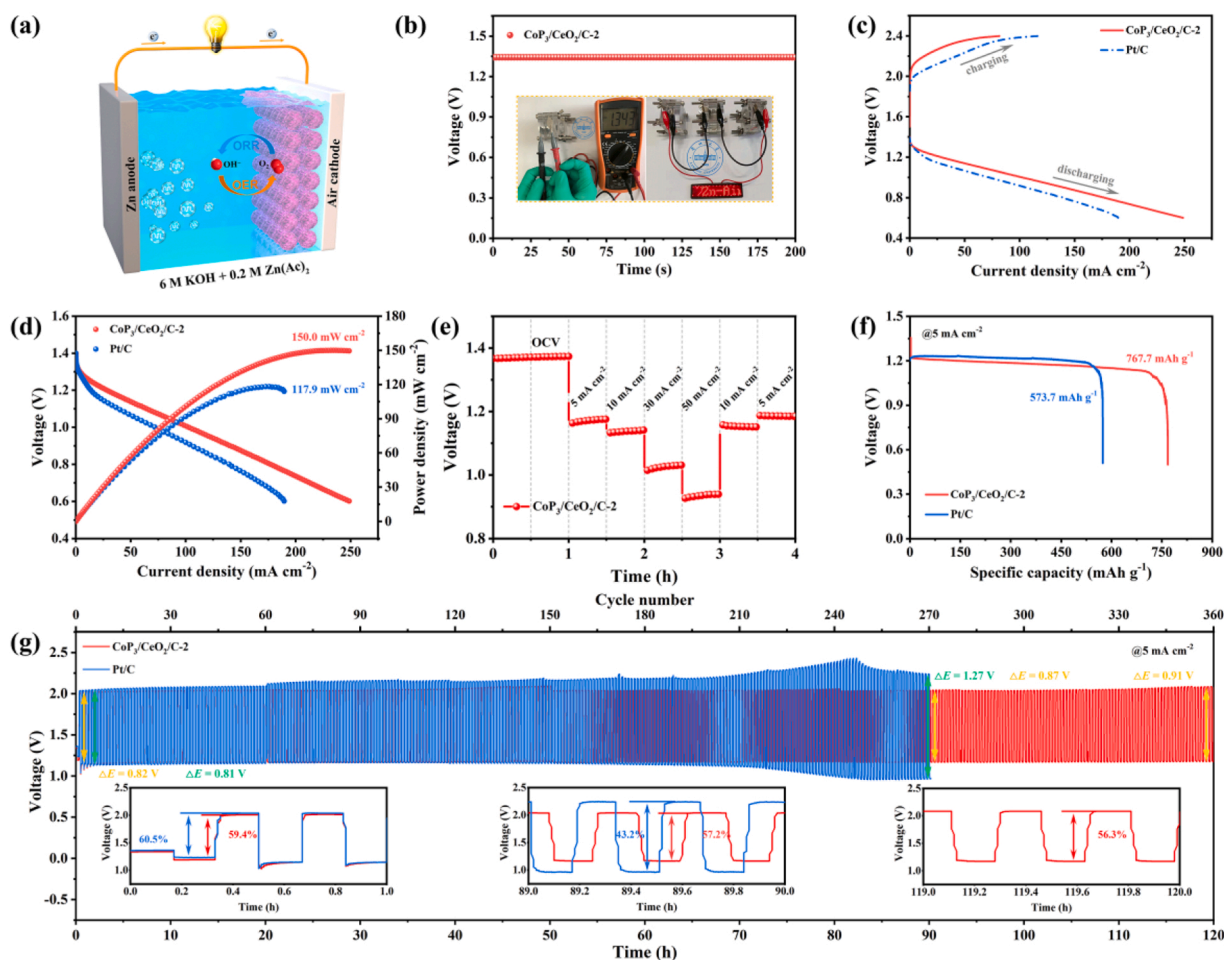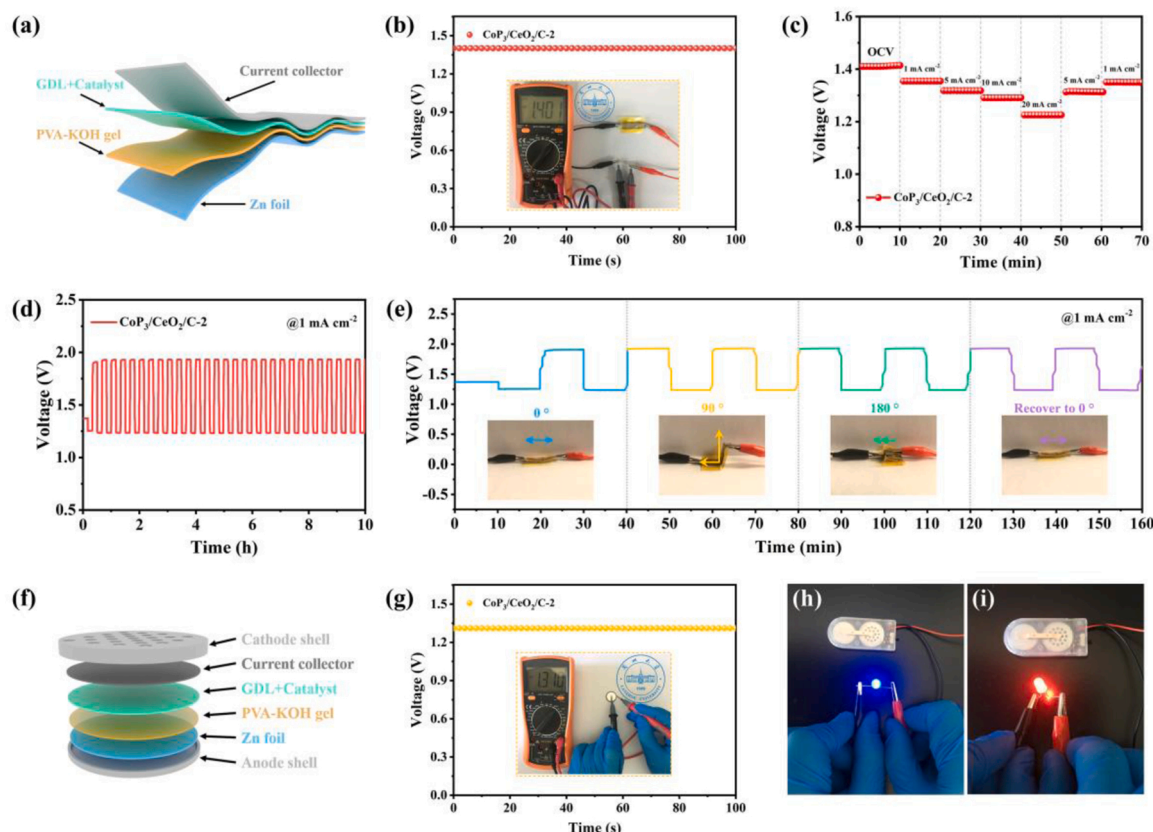
Fig. 7. Electrochemical performance of the aqueous Zn-air batteries with $CoP_3/CeO_2/C$-2 and Pt/C as the air cathodes. (a) Schematic representation of the aqueous Zn-air battery. (b) Open-circuit voltage plot of the $CoP_3/CeO_2/C$-2-based Zn-air battery. Inset: digital photographs of the Zn-air battery measured with a multimeter and a red LED screen powered by three $CoP_3/CeO_2/C$-2-based Zn-air batteries connected in series. (c) Charge and discharge polarization curves. (d) Discharge polarization curves and the corresponding power density of Zn-air batteries. (e) Galvanostatic discharge profiles of the $CoP_3/CeO_2/C$-2-based Zn-air battery at various current densities. (f) Galvanostatic discharge curves of Zn-air batteries at 5 mA cm^{-2}. (g) Galvanostatic charge-discharge cycling curves of Zn-air batteries.

performance [79]. Fig. 7e indicated that the $CoP_3/CeO_2/C$-2-based Zn-air battery had good rate performance with high voltage retention of 99.5 % and 99.6 % at 5 and 10 mA cm^{-2}, respectively, owing to its remarkable reversibility [80]. Moreover, as shown in Fig. 7f, the $CoP_3/CeO_2/C$-2-based Zn-air battery also demonstrated a higher specific capacity of 767.7 mAh g$_{Zn}^{-1}$ at a current density of 5 mA cm^{-2} than Pt/C-based Zn-air battery (573.7 mAh g$_{Zn}^{-1}$). Correspondingly, the energy density of the $CoP_3/CeO_2/C$-2-based and Pt/C-based Zn-air batteries was 871.3 and 651.1 Wh kg$_{Zn}^{-1}$, respectively. The superior energy density of the $CoP_3/CeO_2/C$-2-based Zn-air battery could be explained by the presence of the abundant oxygen vacancies and large specific surface area in the $CoP_3/CeO_2/C$-2 catalyst, which endowed the inner active sites accessible to oxygen and electrolyte, leading to enhanced ORR kinetics [46,81]. Such robust battery performance of $CoP_3/CeO_2/C$-2 surpassed most reported TMPs-based electrocatalysts (Table S6). Furthermore, to evaluate the cycling stability of Zn-air batteries, the galvanostatic charge-discharge cycling tests were performed at a constant current density of 5 mA cm^{-2} (Fig. 7g). Initially, it was found that the $CoP_3/CeO_2/C$-2-based Zn-air battery possessed a large energy efficiency of 59.4 % and a low voltage gap of 0.82 V, which were close to those of the Zn-air battery with Pt/C as the air cathode (60.5 % and 0.81 V). However, the cycling stability of the Pt/C-based Zn-air battery was significantly decreased with a high voltage gap of 1.27 V and a small energy efficiency of 43.2 % after 270 cycles. For the $CoP_3/CeO_2/C$-2-based Zn-air battery, it still exhibited excellent cycling stability with a

slight change of energy efficiency (56.3 %) and voltage gap (0.91 V) over continuous 360 cycles.

The flexible solid-state Zn-air battery was assembled using NF as the current collector, Zn foil as the anode, poly(vinyl alcohol) (PVA)-KOH gel as the electrolyte, and $CoP_3/CeO_2/C$-2 loaded on carbon cloth as the air cathode (Fig. 8a). As depicted in Fig. 8b, the solid-state $CoP_3/CeO_2/C$-2-based Zn-air battery delivered a stable OCV of 1.401 V. Fig. 8c displayed the discharge curves of solid-state Zn-air battery, it was found that the Zn-air battery showed negligible decay in discharge potential at current densities of 1 and 5 mA cm^{-2}, suggesting good rate performance [82]. Moreover, the $CoP_3/CeO_2/C$-2-based Zn-air battery could exhibit good cycling stability at a current density of 1 mA cm^{-2} (Fig. 8d). Even at higher current densities of 50 and 100 mA cm^{-2} (Fig. S27a and b), the $CoP_3/CeO_2/C$-2-based Zn-air battery had stable charge voltages of 2.296 and 2.465 V, respectively, indicating its good stability. As listed in Table S7, the flexible solid-state Zn-air battery with the $CoP_3/CeO_2/C$-2 cathode exhibited small voltage gaps at different current densities, which were superior or comparable to many other reported flexible Zn-air batteries with PVA-based gel electrolytes. When the assembled Zn-air battery was bent to different angles (Fig. 8e), it still maintained stable charge and discharge voltage plateaus, indicating its good flexibility. Further, the coin-type solid-state Zn-air battery was also assembled with $CoP_3/CeO_2/C$-2 as the air cathode (Fig. 8f). As shown in Fig. 7g, a single coin-type Zn-air battery could obtain an OCV of 1.310 V. Besides, the two coin-type Zn-air batteries connected in series could

Fig. 8. Electrochemical performance of the solid-state Zn-air batteries with $CoP_3/CeO_2/C$-2 as the air cathode. (a) Schematic configuration of a flexible solid-state Zn-air battery. (b) Open-circuit voltage plot of the solid-state $CoP_3/CeO_2/C$-2-based Zn-air battery. Inset: digital photograph of the Zn-air battery measured with a multimeter. (c) Galvanostatic discharge curves at various current densities. (d) Galvanostatic charge-discharge cycling plots at 1 mA cm^{-2}. (e) Galvanostatic charge-discharge cycling curves of the solid-state Zn-air battery under different bending angles. (f) Schematic configuration of the coin-type solid-state Zn-air battery. (g) Open-circuit voltage plot of the coin-type solid-state Zn-air battery. Inset: digital photograph of Zn-air battery measured with a multimeter. (h, i) Digital photographs of the (h) blue and (i) red LED lamps powered by two coin-type solid-state Zn-air batteries connected in series.

power blue and red LED lamps (Fig. 8h and i). These results demonstrated the great potential of the solid-state $CoP_3/CeO_2/C$-2-based Zn-air battery in practical battery systems.

3.4. Insights on the heterostructure

To shed light on the role of CoP_3/CeO_2 heterostructure for the enhancement of OER and ORR electrocatalytic activities, the density functional theory (DFT) calculations were performed. Based on the XRD results (Fig. 3a), a model of $CoP_3(211)/CeO_2(111)$ heterojunction was built to elucidate the interaction between CoP_3 and CeO_2 (Fig. S28). As shown in Fig. 9a and b, the charge density difference manifested that significant electron migration from CoP_3 to CeO_2 was observed, leading to the charge accumulation at the interface of CoP_3/CeO_2. This result demonstrated the strong electron coupling effect between CoP_3 and CeO_2 [83]. The electron migration from CoP_3 to CeO_2 also ensured high electron mobility and conductivity at the interface, which facilitated the OER and ORR kinetics [84]. Meanwhile, the formation of a CoP_3/CeO_2 heterojunction could induce charge redistribution at the interface and lower the energy barriers for electrocatalytic reactions, and generate a
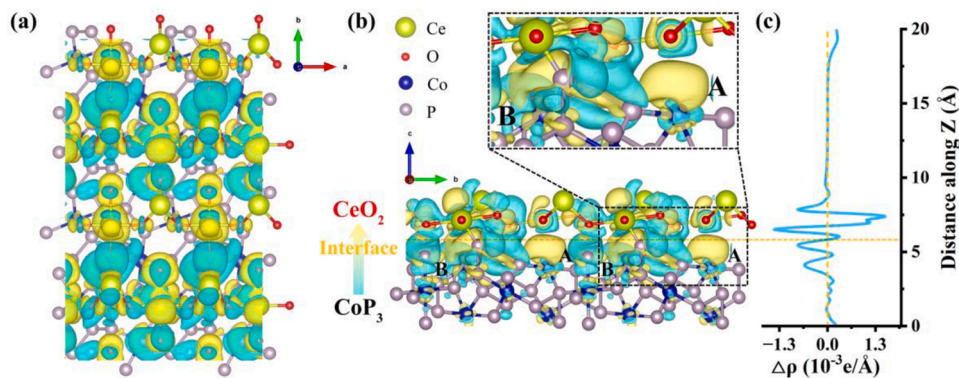
Fig. 9. (a) Top view and (b) side view of the charge density difference distribution at the CoP_3/CeO_2 interface, where the yellow contour represents the charge accumulation and the cyan contour represents the charge depletion. The isosurface value is set to be 0.00131 e/bohr^3. (c) Profile of the planar averaged charge density difference $\Delta\rho$ along the Z-direction for the CoP_3/CeO_2 heterojunction.

favorable electronic microenvironment for OER and ORR [85]. The unique heterostructure could further enhance the surface adsorption/activation/dissociation ability of oxygen intermediates [86]. In addition, the resultant charge redistribution could modulate the electronic structure of the Co atom. Fig. 9b also reflected that the Co atom in the A site gained electrons while the Co atom in the B site lost electrons, but the electron gaining region was larger, indicating that the Co atom eventually gained electrons. The corresponding planar averaged charge density difference (Fig. 9c) further confirmed that the Co atom gained electrons, which was similar to the results reported in the literature [87]. As reported, in the heterostructure of V-CoP/CeO_2, although electron transfer from V-CoP to CeO_2 occurred at the interface, the electron cloud density of the Co atom at the active site was enhanced due to charge redistribution, leading to the formation of low-valence Co species [87]. The abundant low-valence state of Co is more favorable as an active site to improve electrocatalytic activities for OER [87,88]. More importantly, the oxygen vacancies clusters in defective CeO_2 could readily migrate through the "spillover" effect, which was beneficial for improving the activity and stability of the catalyst [89]. Since these migrating oxygen vacancies were accompanied by readily adsorbed reactive oxygen intermediates, this facilitated oxygen electrocatalysis [84]. At the same time, oxygen vacancies could increase the intrinsic conductivity and provide more accessible active sites for promoting OER and ORR [90].

4. Conclusions

In summary, the 3D flower-like $CoP_3/CeO_2/C$ heterostructures were designed via a pyrolysis-phosphorization strategy, and their electrocatalytic properties toward OER and ORR were systematically investigated. The electronic structure, particle size, and morphology of $CoP_3/CeO_2/C$ heterostructures could be modulated by introducing 3D CeO_2 nanoflowers. Among these heterostructures, the $CoP_3/CeO_2/C$-2 catalyst possessed a large surface area, favorable hydrophilicity, and rich oxygen vacancies originating from CoP_3 and CeO_2. These unique structural features of the $CoP_3/CeO_2/C$-2 could generate more accessible active sites and abundant channels for charge/mass transport, leading to superior electrocatalytic activity. More importantly, compared with individual CoP_3/C, the OER and ORR electrocatalytic activities and long-term stabilities of the $CoP_3/CeO_2/C$-2 were significantly improved. Meanwhile, when the $CoP_3/CeO_2/C$-2 was employed as the air cathode for the practical application in the aqueous and solid-state Zn-air batteries, the $CoP_3/CeO_2/C$-2-based Zn-air battery delivered more efficient performance and better cycling stability compared with Pt/C-based Zn-air battery. Besides, an effective approach has been developed to improve the electrocatalytic activity and stability of TMPs.

CRediT authorship contribution statement

Jinmei Li: Methodology, Investigation, Visualization, Data curation, Writing – original draft. **Yumao Kang:** Investigation. **Ziqiang Lei:** Resources. **Peng Liu:** Conceptualization, Resources, Investigation, Writing – review & editing, Supervision.

Declaration of Competing Interest

The authors declare that they have no known competing financial interests or personal relationships that could have appeared to influence the work reported in this paper.

Data availability

Data will be made available on request.

Appendix A. Supporting information

Supplementary data associated with this article can be found in the online version at doi:10.1016/j.apcatb.2022.122029.

References

[1] Y. Zhu, Q. Lin, Y. Zhong, H.A. Tahini, Z. Shao, H. Wang, Metal oxide-based materials as an emerging family of hydrogen evolution electrocatalysts, Energy Environ. Sci. 13 (2020) 3361–3392.

[2] J. Zhang, H. Yang, B. Liu, Coordination engineering of single-atom catalysts for the oxygen reduction reaction: a review, Adv. Energy Mater. 11 (2021), 2002473.

[3] X. Xiao, L. Zou, H. Pang, Q. Xu, Synthesis of micro/nanoscaled metal-organic frameworks and their direct electrochemical applications, Chem. Soc. Rev. 49 (2020) 301–331.

[4] X.F. Lu, Y. Fang, D. Luan, X.W.D. Lou, Metal-organic frameworks derived functional materials for electrochemical energy storage and conversion: a mini review, Nano Lett. 21 (2021) 1555–1565.

[5] L. Yan, Z. Xu, W. Hu, J. Ning, Y. Zhong, Y. Hu, Formation of sandwiched leaf-like CNTs-Co/ZnCo2O4@NC-CNTs nanohybrids for high-power-density rechargeable Zn-air batteries, Nano Energy 82 (2021), 105710.

[6] X.F. Lu, Y. Chen, S. Wang, S. Gao, X.W.D. Lou, Interfacing manganese oxide and cobalt in porous graphitic carbon polyhedrons boosts oxygen electrocatalysis for Zn-air batteries, Adv. Mater. 31 (2019), 1902339.

[7] Z. Yang, C. Zhao, Y. Qu, H. Zhou, F. Zhou, J. Wang, Y. Wu, Y. Li, Trifunctional self-supporting cobalt-embedded carbon nanotube films for ORR, OER, and HER triggered by solid diffusion from bulk metal, Adv. Mater. 31 (2019), 1808043.

[8] Q. Kang, D. Lai, W. Tang, Q. Lu, F. Gao, Intrinsic activity modulation and structural design of NiFe alloy catalysts for an efficient oxygen evolution reaction, Chem. Sci. 12 (2021) 3818–3835.

[9] Y. Yan, C. Liu, H. Jian, X. Cheng, T. Hu, D. Wang, L. Shang, G. Chen, P. Schaaf, X. Wang, E. Kan, T. Zhang, Substitutionally dispersed high-oxidation CoOx clusters in the lattice of rutile TiO2 triggering efficient Co-Ti cooperative catalytic centers for oxygen evolution reactions, Adv. Funct. Mater. 31 (2021), 2009610.

[10] S. Niu, X.-P. Kong, S. Li, Y. Zhang, J. Wu, W. Zhao, P. Xu, Low Ru loading RuO2/(Co,Mn)3O4 nanocomposite with modulated electronic structure for efficient oxygen evolution reaction in acid, Appl. Catal. B Environ. 297 (2021), 120442.

[11] L.S. Bezerra, G. Maia, Developing efficient catalysts for the OER and ORR using a combination of Co, Ni, and Pt oxides along with graphene nanoribbons and NiCo2O4, J. Mater. Chem. A 8 (2020) 17691–17705.

[12] K. Song, Y. Feng, W. Zhang, W. Zheng, MOFs fertilized transition-metallic single-atom electrocatalysts for highly-efficient oxygen reduction: spreading the synthesis strategies and advanced identification, J. Energy Chem. 67 (2022) 391–422.

[13] D. Liu, J.C. Li, S. Ding, Z. Lyu, S. Feng, H. Tian, C. Huyan, M. Xu, T. Li, D. Du, P. Liu, M. Shao, Y. Lin, 2D single-atom catalyst with optimized iron sites produced by thermal melting of metal-organic frameworks for oxygen reduction reaction, Small Methods 4 (2020), 1900827.

[14] Q. Lu, X. Zou, X. Bu, K. Liao, W. Zhou, Z. Shao, A controllable dual interface engineering concept for rational design of efficient bifunctional electrocatalyst for zinc-air batteries, Small 18 (2022), 2105604.

[15] C.X. Zhao, J.N. Liu, J. Wang, C. Wang, X. Guo, X.Y. Li, X. Chen, L. Song, B.Q. Li, Q. Zhang, A clicking confinement strategy to fabricate transition metal single-atom sites for bifunctional oxygen electrocatalysis, Sci. Adv. 8 (2022) eabn5091.

[16] Y. Feng, K. Song, W. Zhang, X. Zhou, S.J. Yoo, J.-G. Kim, S. Qiao, Y. Qi, X. Zou, Z. Chen, T. Qin, N. Yue, Z. Wang, D. Li, W. Zheng, Efficient ORR catalysts for zinc-air battery: biomass-derived ultra-stable Co nanoparticles wrapped with graphitic layers via optimizing electron transfer, J. Energy Chem. 70 (2022) 211–218.

[17] Z.-C. Yao, T. Tang, J.-S. Hu, L.-J. Wan, Recent advances on nonprecious-metal-based bifunctional oxygen electrocatalysts for zinc-air batteries, Energy Fuels 35 (2021) 6380–6401.

[18] H. Zhang, A.W. Maijenburg, X. Li, S.L. Schweizer, R.B. Wehrspohn, Bifunctional heterostructured transition metal phosphides for efficient electrochemical water splitting, Adv. Funct. Mater. 30 (2020), 2003261.

[19] X.F. Lu, L. Yu, X.W.D. Lou, Highly crystalline Ni-doped FeP/carbon hollow nanorods as all-pH efficient and durable hydrogen evolving electrocatalysts, Sci. Adv. 5 (2019) eaav6009.

[20] Y.S. Wei, M. Zhang, M. Kitta, Z. Liu, S. Horike, Q. Xu, A single-crystal open-capsule metal-organic framework, J. Am. Chem. Soc. 141 (2019) 7906–7916.

[21] Y. Shi, M. Li, Y. Yu, B. Zhang, Recent advances in nanostructured transition metal phosphides: synthesis and energy-related applications, Energy Environ. Sci. 13 (2020) 4564–4582.

[22] B. Yang, J. Xu, D. Bin, J. Wang, J. Zhao, Y. Liu, B. Li, X. Fang, Y. Liu, L. Qiao, L. Liu, B. Liu, Amorphous phosphatized ruthenium-iron bimetallic nanoclusters with Pt-like activity for hydrogen evolution reaction, Appl. Catal. B Environ. 283 (2021), 119583.

[23] B. Deng, L. Zhou, Z. Jiang, Z.-J. Jiang, High catalytic performance of nickel foam supported Co2P-Ni2P for overall water splitting and its structural evolutions during hydrogen/oxygen evolution reactions in alkaline solutions, J. Catal. 373 (2019) 81–92.

[24] M. Wu, G. Zhang, N. Chen, Y. Hu, T. Regier, D. Rawach, S. Sun, Self-reconstruction of Co/Co2P heterojunctions confined in N-doped carbon nanotubes for zinc-air flow batteries, ACS Energy Lett. 6 (2021) 1153–1161.

[25] W. Li, Y. Jiang, Y. Li, Q. Gao, W. Shen, Y. Jiang, R. He, M. Li, Electronic modulation of CoP nanoarrays by Cr-doping for efficient overall water splitting, Chem. Eng. J. 425 (2021), 130651.

[26] Y. Wang, M. Wu, J. Li, H. Huang, J. Qiao, In situ growth of CoP nanoparticles anchored on (N,P) co-doped porous carbon engineered by MOFs as advanced bifunctional oxygen catalyst for rechargeable Zn-air battery, J. Mater. Chem. A 8 (2020) 19043–19049.

[27] Y. Wang, Y. Jiao, H. Yan, G. Yang, C. Tian, A. Wu, Y. Liu, H. Fu, Vanadium-incorporated CoP_2 with lattice expansion for highly efficient acidic overall water splitting, Angew. Chem. Int. Ed. 61 (2022), 202116233.

[28] Y. Cheng, Y. Pei, P. Zhuang, H. Chu, Y. Cao, W. Smith, P. Dong, J. Shen, M. Ye, P. M. Ajayan, Precursor-transformation strategy preparation of CuP_x nanodots-decorated CoP_3 nanowires hybrid catalysts for boosting pH-universal electrocatalytic hydrogen evolution, Small 15 (2019), 1904681.

[29] M. Li, X. Pan, M. Jiang, Y. Zhang, Y. Tang, G. Fu, Interface engineering of oxygen-vacancy-rich CoP/CeO_2 heterostructure boosts oxygen evolution reaction, Chem. Eng. J. 395 (2020), 125160.

[30] H. Yan, C. Tian, L. Wang, A. Wu, M. Meng, L. Zhao, H. Fu, Phosphorus-modified tungsten nitride/reduced graphene oxide as a high-performance, non-noble-metal electrocatalyst for the hydrogen evolution reaction, Angew. Chem. Int. Ed. 54 (2015) 6325–6329.

[31] T. Wu, M. Pi, D. Zhang, S. Chen, 3D structured porous CoP_3 nanoneedle arrays as an efficient bifunctional electrocatalyst for the evolution reaction of hydrogen and oxygen, J. Mater. Chem. A 4 (2016) 14539–14544.

[32] J. Zhang, Y. Liu, J. Zhang, Y. Zhang, S. Yuan, D. Wang, J. Lian, Q. Jiang, G. Wang, A self-supporting bifunctional catalyst electrode made of amorphous and porous CoP_3 nanoneedle array: exhaling during overall water splitting, Electrochim. Acta 393 (2021), 138986.

[33] L. Lin, Q. Fu, Y. Han, J. Wang, X. Zhang, Y. Zhang, C. Hu, Z. Liu, Y. Sui, X. Wang, Fe doped skutterudite-type CoP_3 nanoneedles as efficient electrocatalysts for hydrogen and oxygen evolution in alkaline media, J. Alloy. Compd. 808 (2019), 151767.

[34] S. Zhang, M. Guo, S. Song, K. Zhan, Y. Yan, J. Yang, B. Zhao, Hierarchical Mo-doped CoP_3 interconnected nanosheet arrays on carbon cloth as an efficient bifunctional electrocatalyst for water splitting in an alkaline electrolyte, Dalton Trans. 49 (2020) 5563–5572.

[35] M. Sun, H. Liu, J. Qu, J. Li, Earth-rich transition metal phosphide for energy conversion and storage, Adv. Energy Mater. 6 (2016), 1600087.

[36] C.-F. Li, J.-W. Zhao, L.-J. Xie, J.-Q. Wu, G.-R. Li, Fe doping and oxygen vacancy modulated $Fe-Ni_5P_4/NiFeOH$ nanosheets as bifunctional electrocatalysts for efficient overall water splitting, Appl. Catal. B Environ. 291 (2021), 119987.

[37] Y. Liu, C. Ma, Q. Zhang, W. Wang, P. Pan, L. Gu, D. Xu, J. Bao, Z. Dai, 2D electron gas and oxygen vacancy induced high oxygen evolution performances for advanced Co_3O_4/CeO_2 nanohybrids, Adv. Mater. 31 (2019), 1900062.

[38] J. Chen, N. Zhou, H. Wang, Z. Peng, H. Li, Y. Tang, K. Liu, Synergistically enhanced oxygen reduction activity of $MnO_x-CeO_2/Ketjenblack$ composites, Chem. Commun. 51 (2015) 10123–10126.

[39] N. Yao, R. Meng, F. Wu, Z. Fan, G. Cheng, W. Luo, Oxygen-vacancy-induced CeO_2/Co_4N heterostructures toward enhanced pH-universal hydrogen evolution reactions, Appl. Catal. B Environ. 277 (2020), 119282.

[40] Q. Li, L. Song, Z. Liang, M. Sun, T. Wu, B. Huang, F. Luo, Y. Du, C.-H. Yan, A review on CeO_2-based electrocatalyst and photocatalyst in energy conversion, Adv. Energy Sustain. Res. 2 (2021), 2000063.

[41] L. Chen, Y. Zhang, L. Dong, W. Yang, X. Liu, L. Long, C. Liu, S. Dong, J. Jia, Synergistic effect between atomically dispersed Fe and Co metal sites for enhanced oxygen reduction reaction, J. Mater. Chem. A 8 (2020) 4369–4375.

[42] J. Lim, K. Shin, J. Bak, J. Roh, S. Lee, G. Henkelman, E. Cho, Outstanding oxygen reduction reaction catalytic performance of In-PtNi octahedral nanoparticles designed via computational dopant screening, Chem. Mater. 33 (2021) 8895–8903.

[43] H. Cheng, M.-L. Li, C.-Y. Su, N. Li, Z.-Q. Liu, Cu-Co bimetallic oxide quantum dot decorated nitrogen-doped carbon nanotubes: a high-efficiency bifunctional oxygen electrode for Zn-air batteries, Adv. Funct. Mater. 27 (2017), 1701833.

[44] Y. Kang, W. Wang, J. Li, Y. Mi, H. Gong, Z. Lei, 3D Rosa centifolia-like CeO_2 encapsulated with N-doped carbon as an enhanced electrocatalyst for Zn-air batteries, J. Colloid Interface Sci. 578 (2020) 796–804.

[45] Q. Hu, G. Li, X. Liu, B. Zhu, X. Chai, Q. Zhang, J. Liu, C. He, Superhydrophilic phytic-acid-doped conductive hydrogels as metal-free and binder-free electrocatalysts for efficient water oxidation, Angew. Chem. Int. Ed. 58 (2019) 4318–4322.

[46] J. Zhang, X. Dong, W. Xing, Y. Luo, Y. Chen, Y. Xue, C. Zhang, J. Chen, G. Wang, R. Wang, Engineering iron single atomic sites with adjacent ZrO_2 nanoclusters via ligand-assisted strategy for effective oxygen reduction reaction and high-performance Zn-air batteries, Chem. Eng. J. 420 (2021), 129938.

[47] Y. Zhang, J. Yang, Z. Yu, Y. Hou, R. Jiang, J. Huang, F. Yang, S. Yao, L. Gao, W. Tang, Modulating carbon-supported transition metal oxide by electron-giving and electron-absorbing functional groups towards efficient overall water splitting, Chem. Eng. J. 416 (2021), 129124.

[48] D. Wang, H. Xu, P. Yang, L. Xiao, L. Du, X. Lu, R. Li, J. Zhang, M. An, A dual-template strategy to engineer hierarchically porous Fe-N-C electrocatalysts for the high-performance cathodes of Zn-air batteries, J. Mater. Chem. A 9 (2021) 9761–9770.

[49] H. Pan, X. Huang, Z. Lu, Z. Zhang, B. An, D. Wu, T. Wang, X. Chen, F. Cheng, Dual oxidation and sulfurization enabling hybrid $Co/Co_3O_4@CoS$ in S/N-doped carbon matrix for bifunctional oxygen electrocatalysis and rechargeable Zn-air batteries, Chem. Eng. J. 419 (2021), 129619.

[50] Y. Wang, R. Gan, Z. Ai, H. Liu, C. Wei, Y. Song, M. Dirican, X. Zhang, C. Ma, J. Shi, Hollow Co_3O_{4-x} nanoparticles decorated N-doped porous carbon prepared by one-step pyrolysis as an efficient ORR electrocatalyst for rechargeable Zn-air batteries, Carbon 181 (2021) 87–98.

[51] Y. Deng, X. Tian, B. Chi, Q. Wang, W. Ni, Y. Gao, Z. Liu, J. Luo, C. Lin, L. Ling, F. Cheng, Y. Zhang, S. Liao, S. Zhang, Hierarchically open-porous carbon networks enriched with exclusive $Fe-N_x$ active sites as efficient oxygen reduction catalysts towards acidic H_2-O_2 PEM fuel cell and alkaline Zn-air battery, Chem. Eng. J. 390 (2020), 124479.

[52] R. Wang, X.Y. Dong, J. Du, J.Y. Zhao, S.Q. Zang, MOF-derived bifunctional Cu_3P nanoparticles coated by a N,P-codoped carbon shell for hydrogen evolution and oxygen reduction, Adv. Mater. 30 (2018), 1703711.

[53] M. Zhang, Y. Wang, L. Huang, Z. Xu, C. Li, G. Shi, Multifunctional pristine chemically modified graphene films as strong as stainless steel, Adv. Mater. 27 (2015) 6708–6713.

[54] Y. Sun, Y. Guan, X. Wu, W. Li, Y. Li, L. Sun, H. Mi, Q. Zhang, C. He, X. Ren, ZIF-derived "senbei"-like $Co_9S_8/CeO_2/Co$ heterostructural nitrogen-doped carbon nanosheets as bifunctional oxygen electrocatalysts for Zn-air batteries, Nanoscale 13 (2021) 3227–3236.

[55] T. Chen, J. Ma, S. Chen, Y. Wei, C. Deng, J. Chen, J. Hu, W. Ding, Construction of heterostructured CoP/CN/Ni: electron redistribution towards effective hydrogen generation and oxygen reduction, Chem. Eng. J. 415 (2021), 129031.

[56] P. Zhang, Y. Liu, T. Liang, E.H. Ang, X. Zhang, F. Ma, Z. Dai, Nitrogen-doped carbon wrapped $Co-Mo_2C$ dual Mott-Schottky nanosheets with large porosity for efficient water electrolysis, Appl. Catal. B Environ. 284 (2021), 119738.

[57] Y. Yan, J.Y. Zhang, X.R. Shi, Y. Zhu, C. Xia, S. Zaman, X. Hu, X. Wang, B.Y. Xia, A zeolitic-imidazole framework-derived trifunctional electrocatalyst for hydrazine fuel cells, ACS Nano 15 (2021) 10286–10295.

[58] L. Yan, H. Wang, J. Shen, J. Ning, Y. Zhong, Y. Hu, Formation of mesoporous $Co/CoS/Metal-N-C@S$, N-codoped hairy carbon polyhedrons as an efficient trifunctional electrocatalyst for Zn-air batteries and water splitting, Chem. Eng. J. 403 (2021), 126385.

[59] X. He, X. Yi, F. Yin, B. Chen, G. Li, H. Yin, Less active CeO_2 regulating bifunctional oxygen electrocatalytic activity of $Co_3O_4@N$-doped carbon for Zn-air batteries, J. Mater. Chem. A 7 (2019) 6753–6765.

[60] C. Cao, J. Xie, S. Zhang, B. Pan, G. Cao, X. Zhao, Graphene-like $\delta-MnO_2$ decorated with ultrafine CeO_2 as a highly efficient catalyst for long-life lithium-oxygen batteries, J. Mater. Chem. A 5 (2017) 6747–6755.

[61] Y. Yang, T. Yue, Y. Wang, Z. Yang, X. Jin, Effects of morphology on electrocatalytic activity of CeO_2 nanomaterials, Microchem. J. 148 (2019) 42–50.

[62] J. Wang, X. Dong, J. Yang, L. Zhu, W. Zeng, J. Wang, Facile hydrothermal synthesis of 3D flower-like $NiCo_2O_4/CeO_2$ composite as effective oxygen reduction reaction catalyst, J. Mater. Sci. Mater. Electron. 31 (2020) 16600–16608.

[63] Z. Zhang, D. Gao, D. Xue, Y. Liu, P. Liu, J. Zhang, J. Qian, Co and CeO_2 co-decorated N-doping carbon nanofibers for rechargeable Zn-air batteries, Nanotechnology 30 (2019), 395401.

[64] W. Hu, Q. Shi, Z. Chen, H. Yin, H. Zhong, P. Wang, $Co_2N/Co_2Mo_3O_8$ heterostructure as a highly active electrocatalyst for an alkaline hydrogen evolution reaction, ACS Appl. Mater. Interfaces 13 (2021) 8337–8343.

[65] S. Riyajuddin, K. Azmi, M. Pahuja, S. Kumar, T. Maruyama, C. Bera, K. Ghosh, Super-hydrophilic hierarchical Ni-foam-graphene-carbon nanotubes-Ni_2P-CuP_2 nano-architecture as efficient electrocatalyst for overall water splitting, ACS Nano 15 (2021) 5586–5599.

[66] Y. Rao, S. Chen, Q. Yue, Y. Kang, Optimizing the spin states of mesoporous Co_3O_4 nanorods through vanadium doping for long-lasting and flexible rechargeable Zn-air batteries, ACS Catal. 11 (2021) 8097–8103.

[67] J. Zhou, Z. Han, X. Wang, H. Gai, Z. Chen, T. Guo, X. Hou, L. Xu, X. Hu, M. Huang, S.V. Levchenko, H. Jiang, Discovery of quantitative electronic structure-OER activity relationship in metal-organic framework electrocatalysts using an integrated theoretical-experimental approach, Adv. Funct. Mater. 31 (2021), 2102066.

[68] F.-F. Zhang, C.-Q. Cheng, J.-Q. Wang, L. Shang, Y. Feng, Y. Zhang, J. Mao, Q.-J. Guo, Y.-M. Xie, C.-K. Dong, Y.-H. Cheng, H. Liu, X.-W. Du, Iridium oxide modified with silver single atom for boosting oxygen evolution reaction in acidic media, ACS Energy Lett. 6 (2021) 1588–1595.

[69] K. Zeng, W. Li, Y. Zhou, Z. Sun, C. Lu, J. Yan, J.-H. Choi, R. Yang, Multilayer hollow $MnCo_2O_4$ microsphere with oxygen vacancies as efficient electrocatalyst for oxygen evolution reaction, Chem. Eng. J. 421 (2021), 127831.

[70] S.F. Zai, A.Q. Dong, J. Li, Z. Wen, C.C. Yang, Q. Jiang, Low-crystallinity mesoporous NiGaFe hydroxide nanosheets on macroporous Ni foam for high-efficiency oxygen evolution electrocatalysis, J. Mater. Chem. A 9 (2021) 6223–6231.

[71] Z. Wang, W. Xu, X. Chen, Y. Peng, Y. Song, C. Lv, H. Liu, J. Sun, D. Yuan, X. Li, X. Guo, D. Yang, L. Zhang, Defect-rich nitrogen doped Co_3O_4/C porous nanocubes enable high-efficiency bifunctional oxygen electrocatalysis, Adv. Funct. Mater. 29 (2019), 1902875.

[72] N. Kornienko, N. Heidary, G. Cibin, E. Reisner, Catalysis by design: development of a bifunctional water splitting catalyst through an operando measurement directed optimization cycle, Chem. Sci. 9 (2018) 5322–5333.

[73] G. de Falco, M. Florent, A. De Rosa, T.J. Bandosz, Proposing an unbiased oxygen reduction reaction onset potential determination by using a Savitzky-Golay differentiation procedure, J. Colloid Interface Sci. 586 (2021) 597–600.

[74] L. Zong, K. Fan, W. Wu, L. Cui, L. Zhang, B. Johannessen, D. Qi, H. Yin, Y. Wang, P. Liu, L. Wang, H. Zhao, Anchoring single copper atoms to microporous carbon spheres as high-performance electrocatalyst for oxygen reduction reaction, Adv. Funct. Mater. 31 (2021), 2104864.

[75] Y. Lin, K. Liu, K. Chen, Y. Xu, H. Li, J. Hu, Y.-R. Lu, T.-S. Chan, X. Qiu, J. Fu, M. Liu, Tuning charge distribution of FeN$_4$ via external N for enhanced oxygen reduction reaction, ACS Catal. 11 (2021) 6304–6315.

[76] T. Wang, X. Cao, H. Qin, L. Shang, S. Zheng, F. Fang, L. Jiao, P-block atomically dispersed antimony catalyst for highly efficient oxygen reduction reaction, Angew. Chem. Int. Ed. 60 (2021) 21237–21241.

[77] J. Guo, L. Gao, X. Tan, Y. Yuan, J. Kim, Y. Wang, H. Wang, Y.J. Zeng, S.I. Choi, S. C. Smith, H. Huang, Template-directed rapid synthesis of Pd-based ultrathin porous intermetallic nanosheets for efficient oxygen reduction, Angew. Chem. Int. Ed. 60 (2021) 10942–10949.

[78] Y.B. Kang, X. Han, S. Kim, H. Yuan, N. Ling, H.C. Ham, L. Dai, H.S. Park, Structural engineering of ultrathin ReS$_2$ on hierarchically architectured graphene for enhanced oxygen reduction, ACS Nano 15 (2021) 5560–5566.

[79] W. Liu, B. Ren, W. Zhang, M. Zhang, G. Li, M. Xiao, J. Zhu, A. Yu, L. Ricardez-Sandoval, Z. Chen, Defect-enriched nitrogen doped-graphene quantum dots engineered NiCo$_2$S$_4$ nanoarray as high-efficiency bifunctional catalyst for flexible Zn-air battery, Small 15 (2019), 1903610.

[80] J. Qian, T. Wang, Z. Zhang, Y. Liu, J. Li, D. Gao, Engineered spin state in Ce doped LaCoO$_3$ with enhanced electrocatalytic activity for rechargeable Zn-air batteries, Nano Energy 74 (2020), 104948.

[81] H.-F. Wang, C. Tang, Q. Zhang, A review of precious-metal-free bifunctional oxygen electrocatalysts: rational design and applications in Zn-air batteries, Adv. Funct. Mater. 28 (2018), 1803329.

[82] X. Xie, L. Peng, H. Yang, G.I.N. Waterhouse, L. Shang, T. Zhang, MIL-101-derived mesoporous carbon supporting highly exposed Fe single-atom sites as efficient oxygen reduction reaction catalysts, Adv. Mater. 33 (2021), 2101038.

[83] X. Zhuang, Y. Zhou, Z. Jiang, X. Yao, X.-Y. Yu, Synergetic electronic modulation and nanostructure engineering of heterostructured RuO$_2$/Co$_3$O$_4$ as advanced bifunctional electrocatalyst for zinc-air batteries, J. Mater. Chem. A 9 (2021) 26669–26675.

[84] Y. Huang, Y. Liu, Y. Deng, J. Zhang, B. He, J. Sun, Z. Yang, W. Zhou, L. Zhao, Enhancing the bifunctional activity of CoSe$_2$ nanocubes by surface decoration of CeO$_2$ for advanced zinc-air batteries, J. Colloid Interface Sci. 625 (2022) 839–849.

[85] T. Li, J. Yin, D. Sun, M. Zhang, H. Pang, L. Xu, Y. Zhang, J. Yang, Y. Tang, J. Xue, Manipulation of mott-schottky Ni/CeO$_2$ heterojunctions into N-doped carbon nanofibers for high-efficiency electrochemical water splitting, Small (2022), 2106592.

[86] F. Yang, X. Zhang, L. Zhou, S. Lin, X. Cao, J. Jiang, X. Lu, Tuning the interfacial electronic coupling of NiO via CeO$_2$ and nitrogen co-decoration for highly efficient oxygen evolution reaction, Chem. Eng. J. 432 (2022), 134255.

[87] L. Yang, R. Liu, L. Jiao, Electronic redistribution: construction and modulation of interface engineering on CoP for enhancing overall water splitting, Adv. Funct. Mater. 30 (2020), 1909618.

[88] H. Ma, Z. Chen, Z. Wang, C.V. Singh, Q. Jiang, Interface engineering of Co/CoMoN/NF heterostructures for high-performance electrochemical overall water splitting, Adv. Sci. (2022), 2105313.

[89] F. Liang, Y. Yu, W. Zhou, X. Xu, Z. Zhu, Highly defective CeO$_2$ as a promoter for efficient and stable water oxidation, J. Mater. Chem. A 3 (2015) 634–640.

[90] Y. Hou, J. Wang, C. Hou, Y. Fan, Y. Zhai, H. Li, F. Dang, S. Chou, Oxygen vacancies promoting the electrocatalytic performance of CeO$_2$ nanorods as cathode materials for Li-O$_2$ batteries, J. Mater. Chem. A 7 (2019) 6552–6561.